Chapter 5

Additional Thermodynamic Quantities Related to Lattice Vibrations of hcp-Fe[3]

5.1 Introduction

A large theoretical and experimental effort has been dedicated to investigating the structural, thermoelastic, and thermodynamic properties of pure iron at the pressure- and temperature (*PT*) conditions of Earth's core. The properties that have received the most attention from the Earth science community are those that are most closely related to seismic observations, since that is the most direct tool we have for probing the deep Earth. In particular, numerous studies have investigated iron's equation of state (e.g., *Brown and McQueen*, 1982; *Jephcoat et al.*, 1986; *Mao et al.*, 1990; *Wasserman et al.*, 1996; *Stixrude et al.*, 1997; *Dubrovinsky et al.*, 1998; *Dewaele et al.*, 2006; *Sola et al.*, 2009; *Sha and Cohen*, 2010) and sound velocities (e.g., *Jeanloz*, 1979; *Brown and McQueen*, 1986; *Lübbers et al.*, 2000; *Fiquet et al.*, 2001; *Mao et al.*, 2001; *Giefers et al.*, 2002; *Antonangeli et al.*, 2004; *Nguyen and Holmes*, 2004; *Lin et al.*, 2005; *Mao et al.*, 2008), which are closely related to seismic observations of Earth's core. Iron's high-pressure melting behavior has also received a significant amount of attention (e.g., *Brown and McQueen*,

[3] Portions of this chapter are revised from *Murphy et al.* (2011b).

1986; *Boehler et al.*, 1990; *Boehler*, 1993; *Shen et al.*, 1998; *Belonoshko et al.*, 2000; *Ahrens et al.*, 2002; *Alfè et al.*, 2002; *Ma et al.*, 2004; *Nguyen and Holmes*, 2004; *Sola and Alfè*, 2009; *Komabayashi and Fei*, 2010; *Murphy et al.*, 2011a; *Jackson et al.*, 2012), and is related to seismic observations via the disappearance of shear waves in the outer core region, and their reappearance in the inner core. Such observations dictate that the temperature at the inner–core boundary must be equal to the melting temperature of core materials, since the solid inner core and liquid outer core are in contact.

Despite the experimental and theoretical efforts that have been applied to the aforementioned properties, significant uncertainties remain (Section 1.2 and Chapter 6). Therefore, there is still a need for accurately determining the vibrational thermodynamic and thermoelastic properties of ε-Fe with high statistical quality, in order to provide a baseline against which to evaluate the effects of alloying candidate light elements with iron. When combined with seismic observations, such high-statistical quality measurements will be a significant step toward better constraining the identities and amounts of light elements that are present in Earth's core.

To further investigate the properties of Earth's core, there are a number of additional thermodynamic parameters that can be obtained from lattice dynamics. For example, the thermal expansion coefficient of ε-Fe helps to constrain the density of iron under the pressure and temperature (*PT*) conditions of Earth's core and, in turn, the core-density deficit (Section 3.5) (e.g., *Jeanloz*, 1979; *Alfè et al.*, 2001; *Isaak and Anderson*, 2003). In addition, the isotopic partition function ratios of iron provide information about the distribution of heavy iron isotopes during equilibrium processes involving solid iron. We note that the latter parameter is related to lattice dynamics via the fact that the mass of atoms in a crystal influence the frequency of atomic vibrations (phonons) and, in turn, the internal energy of the system.

Here we present the volume dependence of select thermodynamic and thermoelastic parameters of ε-Fe related to lattice vibrations, which we obtained from measurements of its total phonon density of states (DOS) between pressures of 30 and 171 GPa (Chapter 2). In particular, we report experimentally determined values for the volume dependence of ε-Fe's Lamb-Mössbauer factor (f_{LM}); vibrational components of its kinetic energy (E_K) and entropy (S_{vib}); and its Debye sound velocity (v_D). Details for obtaining each parameter from the phonon DOS will be presented in their respective sections.

From our experimentally determined $E_K(V)$, we obtain ε-Fe's reduced isotopic partition function ratios (β-factors), and discuss their utility for investigating iron's equilibrium isotope fractionation based on the available pressure and temperature resolution. In addition, we use our measured $S_{vib}(V)$ to determine the vibrational components of ε-Fe's thermal expansion coefficient and, in turn, investigate the temperature dependence of the thermal pressure and Grüneisen parameter. Finally, we use our measured v_D and existing equation of state parameters (*Dewaele et al.*, 2006) to determine ε-Fe's compressional and shear sound velocities, which we qualitatively compare with seismic observations of Earth's core.

5.2 Lamb-Mössbauer Factor

The Lamb-Mössbauer factor (f_{LM}) represents the probability for recoilless absorption, or the ratio of the elastic to total incoherent scattering in NRIXS experiments. It has a similar functional form as that of the Debye-Waller factor (f_{DW}), where f_{DW} describes coherent, fast scattering events and f_{LM} describes slow scattering events, i.e., events that occur over the lifetime of nuclear resonance (141 ns for ^{57}Fe) (*Sturhahn*, 2004). In general, f_{LM} can best be understood by its relationship to the thermal motion of resonant nuclei about their equilibrium positions (^{57}Fe in our case): $f_{LM} = \exp\left[-k_0^{\,2}\left\langle u^2\right\rangle\right]$, where k_0 is the wavenumber of the resonant x-rays (7.306 Å^{-1} for ^{57}Fe) and $\langle u^2 \rangle$ is the mean square atomic displacement. This relationship highlights the fact that f_{LM} contains information about lattice dynamics and, in turn, depends strongly on the binding of the resonant nuclei in the lattice (e.g., on composition, lattice structure, and pressure and temperature conditions).

There are two ways to access f_{LM} from NRIXS data. First, f_{LM} can be determined from a moments analysis of the pure phonon excitation spectrum, $I'(E)$, which is the spectral shape produced by fitting and subtracting the elastic peak from the measured NRIXS data (*Sturhahn et al.*, 1995). In turn, $I'(E)$ is related to the excitation probability density, $S(E)$, via the previously discussed normalization and refinement procedures (see Section 2.3.3). Finally, f_{LM} is obtained from the total $S(E)$—i.e., the sum of the one- and multi-phonon contributions—by evaluating its 0th-order moment, or $S_n = \int E^n S(E)\, dE$ for $n = 0$. Details of this procedure can be found in *Sturhahn and Chumakov* (1999).

The second method for extracting f_{LM} from NRIXS data is via the measured total phonon DOS, $D(E,V)$, which is obtained by applying a quasi-harmonic lattice model to the total $S(E)$ described above. In particular,

$$f_{LM}(V) = \exp\left[-\int \frac{E_R}{E} \coth\left(\frac{\beta E}{2}\right) D(E,V)\, dE\right], \tag{5.1}$$

where $\beta = (k_B T)^{-1}$ is the inverse temperature, k_B is Boltzmann's constant, and the phonon

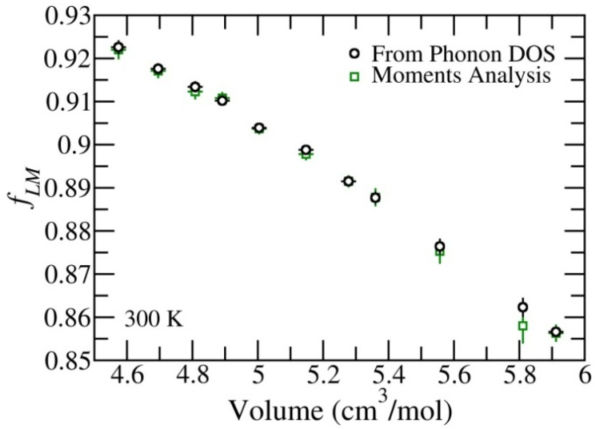

Figure 5.1. Lamb-Mössbauer factor of ε-Fe from NRIXS data. Black circles give the Lamb-Mössbauer factor (f_{LM}) as determined from ε-Fe's total phonon DOS and Equation (5.1). Green squares show f_{LM} as determined from the 0th-order moment of our measured NRIXS data, as described in Section 5.2.

DOS has been normalized by $\int D(E)\,dE = 3$ (*Sturhahn and Jackson*, 2007). Values for f_{LM} determined using Equation (5.1) are given in Table 5.1. We restate the high statistical quality of our dataset by comparing our uncertainties for f_{LM} with those reported by *Mao et al.* (2001) up to 153 GPa. Performing the same PHOENIX analysis on both datasets, we find that our data produce errors in f_{LM} that are ~75% smaller on average using the moments method, and ~60% smaller on average using Equation (5.1).

Values for f_{LM} determined using these two methods are indistinguishable for all of our compression points, as can be seen in Figure 5.1. The most noticeable disagreement in Figure 5.1 occurs at a molar volume per ^{57}Fe atom of 5.81 ± 0.01 cm^3/mol—the compression point at which we had the lowest overall counts based on fewer scans collected (Table 2.2)—which demonstrates the importance of a high-statistical quality dataset for accurately determining vibrational thermodynamic parameters. We note that the two methods are intimately related via $S(E)$, but obtaining f_{LM} from the moments analysis requires no assumptions, while obtaining f_{LM} from Equation (5.1) involves the assumption that a quasi-harmonic oscillator model accurately describes the behavior of ε-Fe. Good agreement between f_{LM} determined from the two distinct methods is consistent with the validity of the quasi-harmonic model over our experimental conditions.

5.3 Kinetic Energy and its Relation to the *β*-Factors of ε-Fe

The vibrational internal energy per ^{57}Fe atom (U_{vib}) can be obtained directly from the integrated phonon DOS, as previously demonstrated in Equation (4.2). In turn, U_{vib} is made up of equal parts kinetic and potential energies in the harmonic lattice approximation, so the vibrational kinetic energy per ^{57}Fe atom (E_K) is given by:

$$E_K\left(V\right)=\frac{1}{4}\int E\coth\frac{\beta E}{2}D\left(E,V\right)dE \tag{5.2}$$

(Table 5.1), where the phonon DOS has been normalized by $\int D\left(E\right)dE=3$. In addition, E_K can be obtained from the 2nd-order moment of $S(E)$, in a procedure similar to that described in the Section 5.2. Values for E_K determined from Equation (5.2) and the moments analysis method are plotted together in Figure 5.2. For all compression points, the values agree within uncertainty, but the moments analysis produces more scatter than Equation (5.2). In addition, the scatter in $E_K(V)$ produced by the moments analysis is larger than that produced in the corresponding determination of f_{LM} (Section 5.2). This is a result of the fact that the kinetic energy arises from a higher-order moment, which amplifies the high-energy region of the measured NRIXS data where counting rates are inherently low and, in turn, statistical fluctuations result in larger uncertainties. Finally, for comparison, we also include in Figure 5.2 the results of our PHOENIX analysis of the NRIXS data measured by *Mao et al.* (2001) up to 153 GPa.

Values for U_{vib} determined using Equation (5.2) were previously reported in Chapter 4 (Table 4.1), where they were used to relate the vibrational Grüneisen parameter to the vibrational thermal pressure using a Mie-Grüneisen type relationship. Here we use the kinetic energy component of the vibrational internal energy to evaluate ε-Fe's reduced

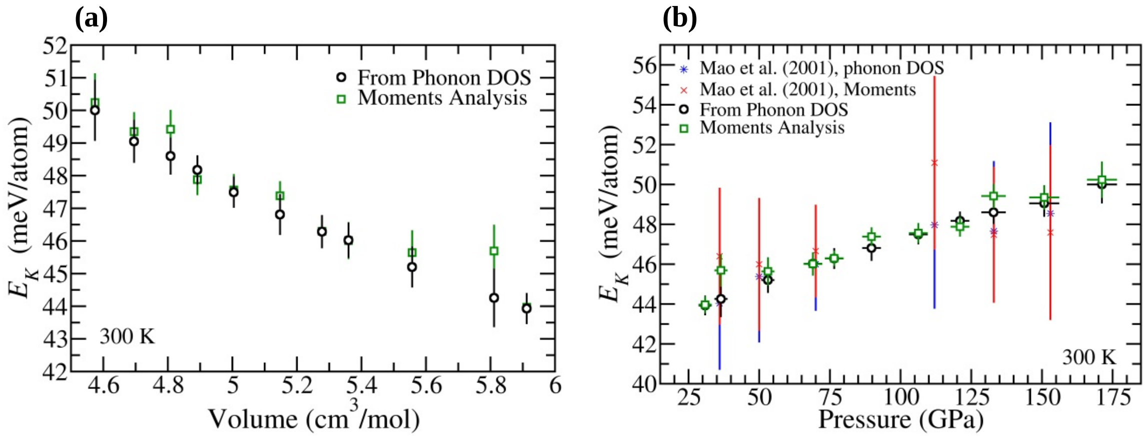

Figure 5.2. Vibrational kinetic energy of ε-Fe from NRIXS data. (a) Black circles give the volume dependence of the vibrational kinetic energy (E_K) determined from our total phonon DOS for ε-Fe and Equation (5.2); green squares show E_K determined from the 2nd-order moment of our measured NRIXS data (see related discussion in Section 5.2). (b) Black circles and green squares give the same values for E_K as in Figure 5.2a, but now as a function of pressure, which is determined from our *in situ* XRD and the Vinet EOS parameters reported by *Dewaele et al.* (2006). For comparison, we also plot E_K from our PHOENIX analysis of the NRIXS dataset on ε-Fe measured by *Mao et al.* (2001); blue stars give E_K from their phonon DOS, and red X's give E_K from the 2nd-order moment of their measured NRIXS data.

isotopic partition function ratios (β-factors), which are related to the distribution of isotopes of iron that results from equilibrium processes at elevated pressures. At a given pressure, the β-factor between two isotopes is related to their free energies (F) via

$$\ln\beta = -\frac{F^* - F}{k_B T} + \left(\frac{F^* - F}{k_B T}\right)_{classical}, \tag{5.3}$$

(*Bigeleisen and Mayer*, 1947; *Schauble*, 2004) where k_B is Boltzmann's constant, T is temperature, asterisks denote values for the isotopically substituted form, and the final subscript refers to values from classical mechanics. From first-order thermodynamic perturbation theory, the difference between free energies of substituted and unsubstituted isotopic forms (F^* - F) can be written in terms of E_K and the difference in isotope masses

$$F^* - F = E_K \frac{\Delta m}{m^*}, \tag{5.4}$$

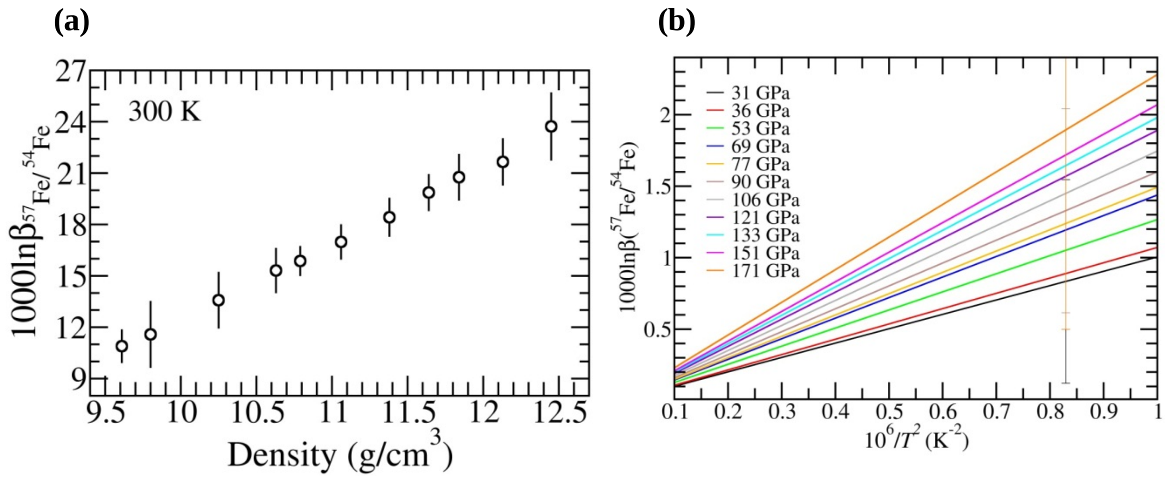

Figure 5.3. Reduced isotopic partition function ratios of ε-Fe. (a) Black circles give the density dependence of the reduced isotopic partition function ratios ($1000\ln\beta_{57Fe/54Fe}$) of ε-Fe at 300 K by the procedure described in Section 5.4. (b) Lines give the temperature dependence of $1000\ln\beta_{57Fe/54Fe}$, with each color corresponding to an individual compression point as labeled in the figure. Error bars for three compression points (31, 90, and 171 GPa) are plotted at T = 1100 K; they reflect the propagation of measured uncertainties for E_K in Equation (5.5).

where $\Delta m = m - m^*$ (i.e., Δm = -3 when ^{57}Fe substitutes for ^{54}Fe) (*Polyakov and Mineev*, 1999). Together with the classical mechanics value of the kinetic energy, which is equal to $3k_BT/2$, Equations (5.3) and (5.4) can be combined to obtain

$$\ln\beta = -\left(\frac{E_K}{k_BT} - \frac{3}{2}\right)\frac{\Delta m}{m^*}. \tag{5.5}$$

Finally, we apply our measured $E_K(V)$ to Equation (5.5) in order to determine the β-factors of ε-Fe for each of our compression points and at 300 K (Table 5.1). In addition, the temperature dependence of Equation (5.5) allows us to explore the effects of temperature on the β-factors of ε-Fe (Figure 5.3), assuming the quasi-harmonic model accurately describes the vibrational behavior of ε-Fe at the relevant PT conditions. The accuracy of the quasi-harmonic model for ε-Fe at high-temperature conditions is unknown (see Section 3.5 for more discussion), but due to the lack of sufficient data on the temperature dependence of ε-Fe's phonon DOS, we will apply it to the discussion in Section 5.6.

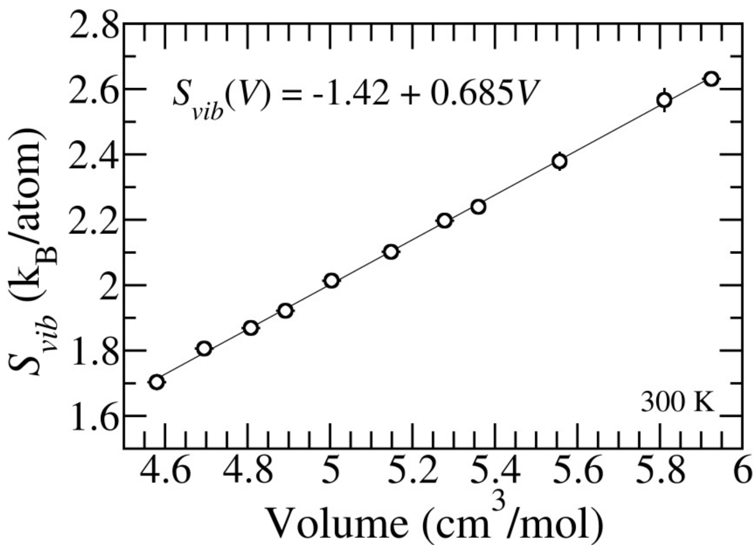

Figure 5.4. Vibrational entropy of ε-Fe. Black circles give the vibrational entropy (S_{vib}) at each compression point and at 300 K (Equation (5.6)); the black line gives the errors-weighted linear fit of our data, the result of which is given on the figure. We note that the reported slope of 0.685 (k_B/atom)/(cm^3/mol) is equivalent to the value given in the text via a conversion of units.

5.4 Entropy and its Relation to the Thermal Expansion Coefficient of ε-Fe

The vibrational entropy per ^{57}Fe atom (S_{vib}) at 300 K can be obtained directly from the integrated phonon DOS via

$$S_{vib} = \frac{k_B \beta}{2} \int E \coth \frac{\beta E}{2} D(E,V)\, dE - k_B \int \ln\left(2 \sinh \frac{\beta E}{2}\right) D(E,V)\, dE \qquad (5.6)$$

(Table 5.1), where the phonon DOS has been normalized by $\int D(E)\, dE = 3$ (*Sturhahn*, 2004). Values for S_{vib} determined from Equation (5.6) as a function of our *in situ* measured volumes are plotted in Figure 5.4, where one can see that S_{vib} decreases roughly linearly with decreasing volume.

The volumetric derivative of S_{vib} at constant temperature is directly related to the vibrational component of the thermal expansion coefficient (α_{vib}) via thermodynamic definition:

$$\left(\frac{\partial S_{vib}}{\partial V}\right)_T = \alpha_{vib} K_T, \qquad (5.7)$$

where K_T is the isothermal bulk modulus. Since our $S_{vib}(V)$ is approximately linear, our

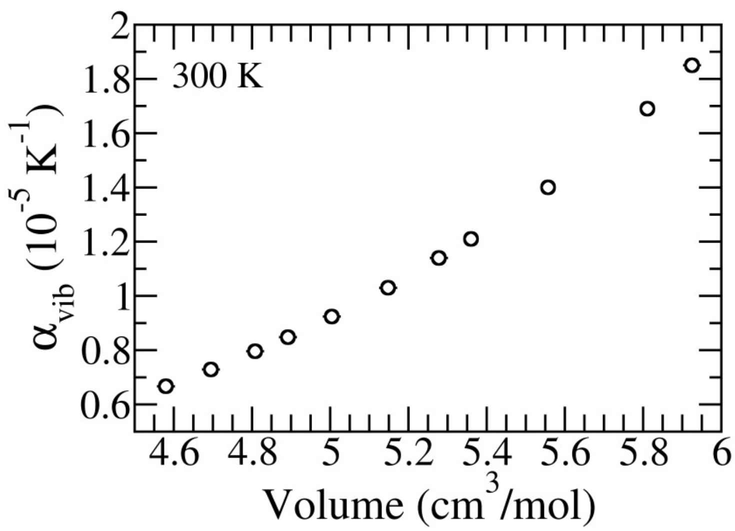

Figure 5.5. Vibrational thermal expansion coefficient of ε-Fe at 300 K. The volume dependence of the vibrational component of the thermal expansion coefficient (α_{vib}) was determined using our measured $S_{vib}(V)$, Equation (5.7), and established EOS parameters from *Dewaele et al.* (2006).

results are consistent with the suggestion that the product $\alpha_{vib}K_T$ is approximately independent of volume at constant temperature. Therefore, taking the derivative of an error-weighted linear fit of our measured $S_{vib}(V)$, we find $\left(\partial S_{vib}/\partial V\right)_{300\text{ K}} = \alpha_{vib}K_T = 5.70 \pm 0.05$ MPa/K. We note that the slope given in Figure 5.4 is equivalent to the slope given here via a conversion of units. For comparison, the corresponding electronic component for ε-Fe was calculated to be $\alpha_{el}K_T \sim 0.25$ MPa/K, which is a factor of 20 smaller than the vibrational component at 300 K (*Wasserman et al.*, 1996).

Applying our $\left(\partial S_{vib}/\partial V\right)_{300\text{ K}}$ result and $K_T(V)$ from the Vinet equation of state (EOS) parameters for ε-Fe reported by *Dewaele et al.* (2006), we find $\alpha_{vib}(300\text{ K}) = 1.84 \pm 0.02$ 10^{-5} K^{-1} and 0.67 ± 0.01 10^{-5} K^{-1} at 30 GPa and 171 GPa, respectively, where reported errors reflect the uncertainties associated with our fitting procedure (Table 5.1; Figure 5.5). Our $\alpha_{vib}(V)$ agrees well with the results from first principles calculations by *Sha and Cohen* (2010a); based on their Figure 6, we approximate their $\alpha_{vib}(300\text{ K}) = 0.9 \times 10^{-5}$ K^{-1} and 0.6×10^{-5} K^{-1} at 100 GPa and 200 GPa, respectively. In addition, our $\alpha_{vib}(V)$

agrees fairly well with the results of shock-compression experiments by *Jeanloz* (1979) at larger compression (see Figure 2 in reference). Based on his reported fitting equations for the bulk modulus and α along the Hugoniot ($K_{S,H}$ and α_H, respectively), *Jeanloz* (1979) found α_H(90 GPa) = 1.2 × 10^{-5} K^{-1} and α_H(171 GPa) = 0.7 × 10^{-5} K^{-1}. However, at smaller compressions, our values disagree by more than uncertainties, with their reported α_H(31 GPa) = 2.6 × 10^{-5} K^{-1}. This large discrepancy at small compressions may be due to the different experimental conditions, i.e., shock-compression experiments are adiabatic, whereas our experiments are isothermal. Finally, considering the fact that electronic and temperature effects are included in α_H—both of which should positively contribute to α—the agreement between our results and those of *Jeanloz* (1979) suggests α is only weakly dependent on temperature, particularly at larger compressions.

This argument is inconsistent with the conclusions of *Alfè et al.* (2001) and *Wasserman et al.* (1996), both of whom found $\alpha_{vib}K_T$ to have a significant dependence on temperature. For example, *Wasserman et al.* (1996) report that at a pressure of 58 GPa, their $\alpha_{vib}K_T$ decreases by ~10% between T = 1000 and 6000 K due to anharmonic effects, but their overall αK_T increases by 40% as a result of the rapidly increasing electronic contribution. We note that our $\alpha_{vib}(V$, 300 K) is indeed smaller than their plotted $\alpha_{vib}(V)$ at elevated temperatures ($T \geq$ 1000 K; see Figures 11 and 8 in references, respectively), but a quantitative comparison at 300 K is not straightforward from their figures alone.

Finally, our $\alpha_{vib}(V)$ is approximately half as large as $\alpha(V)$ reported by *Anderson et al.* (2001) and *Isaak and Anderson* (2003). These two earlier studies are related, and are both based on the differentiation of previously reported high-*PT* XRD data that was collected for ε-Fe up to 305 GPa and 1370 K (*Dubrovinsky et al.*, 2000b). As a result, their reported values are nearly identical with one another. Comparing their reported values with our measurements at the most similar molar volumes per atom, *Isaak and Anderson* (2003) found α(5.9 cm^3/mol) = 3.88 × 10^{-5} K^{-1} and α(4.9 cm^3/mol) = 1.61 × 10^{-5} K^{-1}, both of which are roughly twice as large as our measured values. We acknowledge that investigations of α from XRD include the electronic component, to which our measurements are insensitive. However, based on the high-statistical quality of our dataset and $\alpha_{el}K_T$ ~ 0.25 MPa/K at 300 K reported by *Wasserman et al.* (1996) (see Figure 8 in reference), we conclude that the our results do not agree with those of *Anderson et al.* (2001) and *Isaak and Anderson* (2003).

5.5 Sound Velocities

A parabolic fit of the low-energy region of ε-Fe's phonon DOS provides its Debye sound velocity (v_D), which reflects a weighted average of its compressional (v_p) and shear (v_s) sound velocities (*Hu et al.*, 2003; *Sturhahn and Jackson*, 2007). Therefore, we determined v_D for ε-Fe by using an exact relation for the dispersion of low-energy acoustic phonons and our measured density at each compression point, the latter of which is based on our *in situ* measured volumes and m = 56.95 for 95% isotopically enriched ^{57}Fe (Table 2.1). The appropriate energy range over which to perform each parabolic fit was first estimated from visual inspection of our data, and ultimately determined for each fit via χ^2 analysis. A typical minimum energy for our fits was 3.5 meV, which corresponds roughly to the width of our measured resolution functions; the maximum energy varied between 16 and 34 meV, with larger energy ranges corresponding to larger compressions (Table 5.1). The v_D for each compression point are given in Table 5.2 and plotted in Figure 5.7. Typical uncertainties are ≤ 1%, with the exception of our measurement at V = 4.70 ± 0.02 cm^3/mol

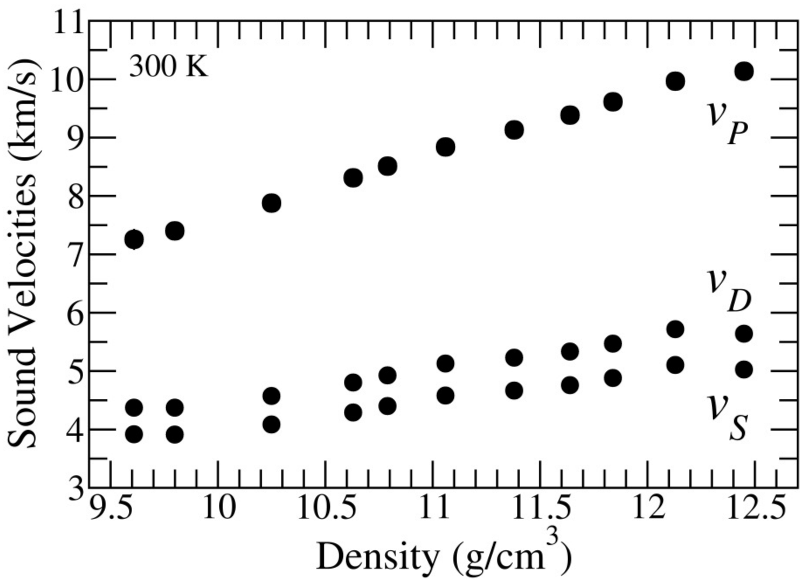

Figure 5.6. Our density-dependent sound velocities at 300 K. Filled black circles give the compressional (v_p) shear (v_s), and Debye (v_D) sound velocities of ε-Fe as a function of density from our NRIXS and *in situ* XRD experiments. Uncertainties in sound velocities and densities are smaller than the symbol if not visible.

(P = 151 ± 5 GPa). The relatively large uncertainty reported at this compression point is the result of a long "tail" on our measured resolution function that extended to approximately −20 meV (Table 5.2).

From our measured v_D and ρ, we determine ε-Fe's compressional (v_p) and shear (v_s) sound velocities via:

$$\frac{K_S}{\rho} = v_P^2 - \frac{4}{3} v_S^2 \tag{5.8}$$

$$\frac{3}{v_D^3} = \frac{1}{v_P^3} + \frac{2}{v_S^3} \tag{5.9}$$

(Table 5.2). The density (ρ) at each compression point is determined from our *in situ* measured volumes, and the adiabatic bulk modulus (K_S) is related to the isothermal bulk modulus (K_T) via $K_S = K_T(1 + \alpha\gamma T)$. Therefore, to determine K_S at each compression point, we scale the ambient temperature K_T reported by *Dewaele et al.* (2006) with the Grüneisen parameter (γ_{vib}) from Section 4.3 (*Murphy et al.*, 2011b) and the vibrational component of

Table 5.1. Vibrational thermodynamic parameters of ε-Fe from the phonon DOS.

V **(cm^3/mol)**[a]	***P*** **(GPa)**[a]	f_{LM}[b]	E_K **(meV/atom)**[b]	$10^3\ln\beta_{57Fe/54Fe}$[c]	S_{vib} **(k$_B$/atom)**[b]	α_{vib} **(10^{-5} K^{-1})**[d]
5.92(2)	30(2)	0.857(1)	43.9(5)	10.9(9)	2.63(2)	1.84(2)
5.81(1)	36(2)	0.862(2)	44.3(9)	11.6(1.9)	2.57(3)	1.69(1)
5.56(1)	53(2)	0.876(2)	45.2(6)	13.6(1.6)	2.38(3)	1.40(1)
5.36(1)	69(3)	0.888(1)	46.0(5)	15.3(1.3)	2.24(2)	1.20(1)
5.27(2)	77(3)	0.892(1)	46.3(5)	15.9(8)	2.20(1)	1.13(1)
5.15(2)	90(3)	0.899(1)	46.8(6)	17.0(1.0)	2.10(1)	1.03(1)
5.00(2)	106(3)	0.904(1)	47.5(4)	18.4(1.1)	2.01(1)	0.92(1)
4.89(2)	121(3)	0.910(1)	48.2(4)	19.9(1.0)	1.92(1)	0.85(1)
4.81(2)	133(4)	0.913(1)	48.6(5)	20.8(1.3)	1.87(2)	0.79(1)
4.70(2)	151(5)	0.918(1)	49.1(6)	21.7(1.3)	1.81(2)	0.73(1)
4.58(2)	171(5)	0.923(1)	50.0(9)	23.7(1.9)	1.70(2)	0.67(1)

[a]Molar volume per ^{57}Fe atom (V) and pressure (P) for each compression point are duplicated from Tables 2.1 and 2.2. A brief explanation of reported uncertainties is given in Section 2.2.
[b]The Lamb-Mössbauer factor (f_{LM}) and vibrational components of the kinetic energy (E_K) and entropy (S_{vib}) per ^{57}Fe atom were determined from the integrated phonon DOS (Equations (5.1), (5.2), and (5.6)). Values in parentheses give uncertainties for the last significant digit reported, as determined by the PHOENIX software (*Sturhahn*, 2000).
[c]Reduced isotopic partition function ratios ($10^3\ln\beta_{57Fe/54Fe}$) for ε-Fe at 300 K are based on our $E_K(V)$ (Equation (5.2)) and the procedure described in Section 5.4; uncertainties in the last significant digit reflect our measured uncertainties in E_K as determined by the PHOENIX software (*Sturhahn*, 2000).
[d]The vibrational component of the thermal expansion coefficient (α_{vib}) for ε-Fe at 300 K is from our $S_{vib}(V)$ (Equation (5.6)) and the Vinet EOS parameters reported by *Dewaele et al.* (2006), as described in Section 5.5; uncertainties in the last significant digit reflect the uncertainties from an error-weighted linear fit of our $S_{vib}(V)$, with uncertainties in S_{vib} determined by the PHOENIX software (*Sturhahn*, 2000).

the thermal expansion coefficient from Section 5.4 (Table 5.1). Using these parameters and including uncertainties in α_{vib} and γ_{vib}, we find $\alpha_{vib}\gamma_{vib}T < 0.01$ over our compression range and at 300 K, thus introducing a difference between K_S and K_T of no more than 1%. In addition, we expect the electronic contributions of α and γ—and, in turn, K_S—to be fairly minor, based on the fact that $\alpha_{el}/\alpha_{vib} \approx 4\%$ (*Wasserman et al.*, 1996), and the electronic contribution to the Grüneisen parameter (weighted by the electronic specific heat capacity) is negligible over this compression range at 300 K (*Boness et al.*, 1986; *Alfè et al.*, 2001).

Table 5.2. Elasticity of ε-Fe from the phonon DOS.

ρ (g/cm³)[a]	**P (GPa)**[a]	**Energy Range (meV)**[b]	**v_D (km/s)**[b]	**K_S (GPa)**[c]	**v_p (km/s)**[c]	**v_s (km/s)**[c]	**μ (GPa)**[c]
9.61(3)	30(2)	3.5 – 16.1	4.36(3)	312	7.27(16)	3.92(3)	147(2)
9.80(1)	36(2)	3.5 – 23.5	4.37(6)	340	7.42(8)	3.91(5)	150(4)
10.25(1)	53(2)	3.5 – 23.5	4.57(4)	411	7.89(8)	4.08(4)	171(3)
10.63(1)	69(3)	3.5 – 23.5	4.80(4)	476	8.33(9)	4.29(4)	196(3)
10.80(2)	77(3)	3.5 – 25.5	4.93(3)	506	8.53(9)	4.40(3)	209(3)
11.06(2)	90(3)	3.5 – 28.4	5.13(3)	558	8.84(9)	4.58(3)	232(3)
11.38(5)	106(3)	3.5 – 28.4	5.23(3)	621	9.14(9)	4.67(3)	248(3)
11.64(2)	121(3)	3.5 – 27.3	5.33(4)	677	9.40(10)	4.76(4)	264(4)
11.84(2)	133(4)	3.5 – 31.2	5.47(5)	721	9.62(11)	4.88(5)	282(6)
12.13(3)	151(5)	9.7 – 32.7	5.72(10)	786	9.98(12)	5.10(9)	316(11)
12.43(3)	171(5)	3.5 – 33.8	5.64(7)	859	10.14(12)	5.03(6)	314(8)

[a]Density (ρ) and pressure (P) for each compression point are duplicated from Tables 2.1 and 2.2. A brief explanation of reported uncertainties is given in Section 2.2.
[b]The best energy range over which the phonon DOS was fit to determine the Debye sound velocity (v_D) was determined by χ^2 analysis; v_D at each compression point depends on our *in situ* measured volumes (densities) and accounts for ^{57}Fe enrichment levels.
[c]The adiabatic bulk modulus (K_S) was determined from the relationship $K_S = K_T(1 + \alpha\gamma T)$, with the isothermal bulk modulus (K_T) reported by *Dewaele et al.* (2006) (Table 2.1), our α_{vib} from Table 5.1 and our γ_{vib} from Section 4.3 (*Murphy et al.*, 2011b), as described in Section 5.5. In turn, K_S was used with our ρ and $v_D(V)$ to determine the compressional (v_p) and shear (v_s) sound velocities and the shear modulus (μ) for ε-Fe using Equations (5.8) and (5.9). Reported uncertainties in the last significant digit reflect uncertainties determined by the PHOENIX software (*Sturhahn*, 2000). We note that uncertainties are not given for K_S because they would largely reflect uncertainties in the EOS parameters reported by *Dewaele et al.* (2006); in particular, our uncertainties in α_{vib} and γ_{vib} contribute an error of only 0.2 GPa.

Applying these values for K_S and our measured ρ and v_D to Equations (5.8) and (5.9), we determined v_p and v_s at each of our compression points (Table 5.2, Figure 5.6). We note that v_p and v_s determined using K_S and K_T at each compression point are identical within uncertainty. Comparisons with previously reported measurements of ε-Fe's $v_D(P)$ and $v_p(P)$—from NRIXS and inelastic x-ray scattering (IXS) experiments at 300 K and up to 153 GPa (*Mao et al.*, 2001; *Giefers et al.*, 2002; *Antonangeli et al.*, 2004; *Lin et al.*, 2005; *Mao et al.*, 2008)—are presented in Figures 5.7 and 5.8, respectively. We do not

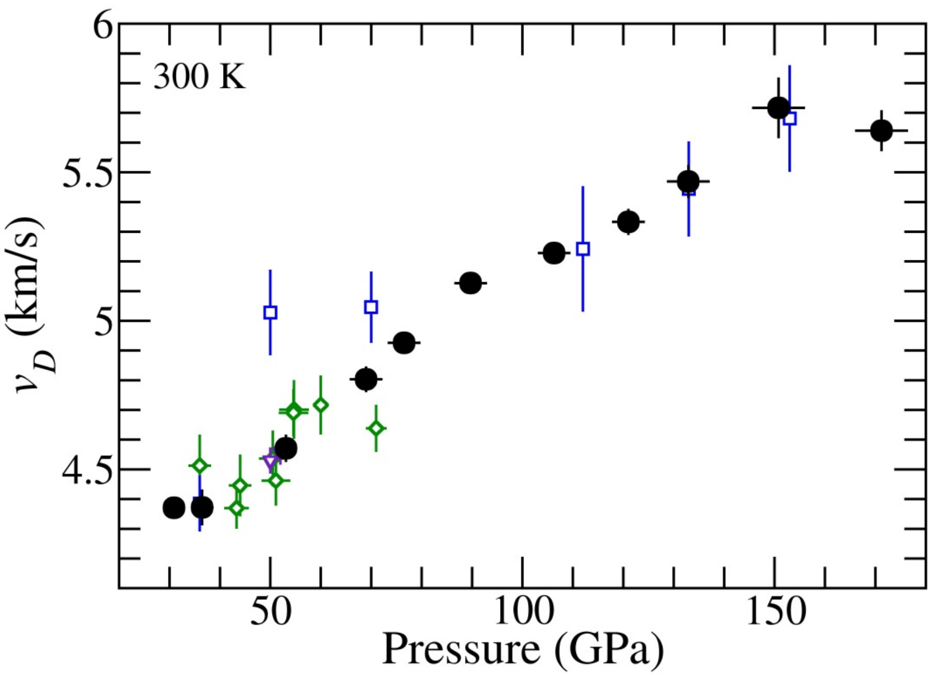

Figure 5.7. Debye sound velocities of ε-Fe at 300 K. Filled black circles give our Debye sound velocities as a function of pressure, $v_D(P)$, where our measured volumes have been converted to pressures using the Vinet EOS parameters reported by *Dewaele et al.* (2006), in order to facilitate comparison with previous studies (unfilled circles). Also plotted are $v_D(P)$ reported by *Mao et al.* (2001) (blue squares); *Lin et al.* (2005) (green diamonds); and *Mao et al.* (2008) (purple down-triangles). We note that we do not include reported values from *Lübbers et al.* (2000) because the energy scale used in that study was incorrect. In addition, we do not include reported values from *Giefers et al.* (2002) because they performed their NRIXS experiments on a purposefully textured sample, with the DAC oriented at an angle relative to the beam; without *in situ* XRD, it is difficult to know the true volume (pressure) of their measured data points.

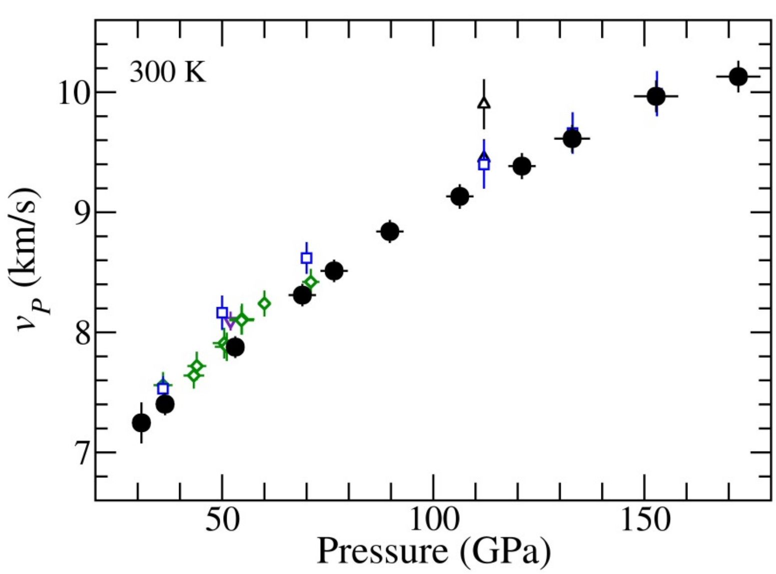

Figure 5.8. Compressional sound velocities of ε-Fe at 300 K. Filled black circles give our compressional sound velocities as a function of pressure, $v_p(P)$. Also plotted are $v_p(P)$ from NRIXS experiments conducted by *Mao et al.* (2001) (blue squares); *Lin et al.* (2005) (green diamonds); and *Mao et al.* (2008) (purple down-triangles). Finally, we plot as black triangles v_p(112 GPa) from an inelastic x-ray scattering (IXS) study by *Antonangeli et al.* (2004).

present a similar comparison for v_s because it would be similar to Figure 5.7, since v_D and v_s from NRIXS experiments are closely related (Equation (5.9)), and the reported IXS experiments on polycrystalline ε-Fe are not sensitive to v_s.

As can be seen in Figures 5.7 and 5.8, our results at smaller compressions are similar to previous NRIXS and IXS measurements. However, the large compression range and high statistical quality of our data provide a new, tight constraint on the density dependence of ε-Fe's sound velocities to an outer core pressure of 171 GPa. In particular, performing the same PHOENIX analysis on datasets reported by *Mao et al.* (2001) and *Lin et al.* (2005), we find that our data produce errors in v_D that are ~60% smaller and ~30% smaller, respectively. Finally, we note that there is no resolvable discontinuity in our measured sound velocities for NRIXS experiments performed in the neon ($P \leq 69$ GPa) and boron-epoxy pressure-transmitting media (Table 2.1).

5.6 Discussion

The high-statistical quality of our phonon DOS and, in turn, the previously discussed parameters, provide a new tight constraint on the Lamb-Mössbauer factor, β-factors, thermal expansion coefficient, and sound velocities of ε-Fe. In the following subsections, we discuss applications of each parameter in the context of Earth's core.

5.6.1 Melting Behavior from f_{LM}

As previously stated, the Lamb-Mössbauer factor (f_{LM}) can best be understood in the context of lattice dynamics by considering the relationship $f_{LM} = \exp\left[-k_0^{\,2}\left\langle u^2\right\rangle\right]$. From this relationship, we see that the steady increase in f_{LM} with compression corresponds to a reduction of thermal motion—i.e., reduced displacement of the iron atoms, or stiffening of the lattice—which is consistent with the expected decrease in $<u^2>$ with increasing compression. We have previously used this behavior to predict a melting curve shape (Section 3.4) based on Gilvarry's reformulation of Lindemann's melting criterion (*Gilvarry*, 1956b; a; *Murphy et al.*, 2011a), which we calibrated in *PT* space with previously reported melting points for ε-Fe (*Shen et al.*, 1998; *Ma et al.*, 2004; *Komabayashi and Fei*, 2010; *Jackson et al.*, 2012). In particular, the values of f_{LM} given in Table 5.1 are closely related to those for the Lamb-Mössbauer temperature (Table 3.1), which was derived from a high-temperature formulation for $<u^2>$ in Equation (3.7). For details of this relationship, see Section 3.4.

5.6.2 Other Thermodynamic Parameters from α_{vib}

The product $\alpha_{vib}K_T$ is related to a number of other parameters via thermodynamic definitions. For example, $\alpha_{vib}K_T$ directly gives the temperature derivative of the vibrational thermal pressure via

$$\alpha_{vib}K_T = \left[\frac{1}{V}\left(\frac{\partial V}{\partial T}\right)_P\right]\left[-V\left(\frac{\partial P}{\partial V}\right)_T\right] = \left(\frac{\partial P_{vib}}{\partial T}\right)_V, \tag{5.10}$$

where the negative sign in the central equation is cancelled by Maxwell's relations and the chain rule. Taking the average temperature derivative of the harmonic component of the vibrational thermal pressure (P_{vib}^h) we determined in Chapter 3, we find that $\alpha_{vib}K_T$ depends on temperature. Therefore, we performed an errors-weighted quadratic fit our $P_{vib}^h(V,T)$ at each of our compression points between T = 100 and 1000 K (see Section 3.3). Taking the derivative of these quadratic fits, we found $\alpha_{vib}K_T$(300 K) = 5.5 ± 0.2 MPa/K, which agrees well with the value determined here of $\alpha_{vib}K_T$(300 K) = 5.70 ± 0.05 MPa/K. We attribute the ~3% discrepancy between these two results to the fact that we are comparing the derivatives of two parameters obtained from our experimental data.

In addition, $\alpha_{vib}K_T$ is related to the vibrational Grüneisen parameter (γ_{vib}) via

$$\gamma_{vib} = \frac{\alpha_{vib} K_T V}{C_{vib}}. \tag{5.11}$$

The volume (V) at each compression point is known from our *in situ* XRD measurements, and the vibrational component of the specific heat capacity (C_{vib}) can be obtained from the total phonon DOS via Equation (4.1). Therefore, we can apply these measured values and the volume-derivative of our measured S_{vib} (i.e., $\alpha_{vib}K_T$) to Equation (5.11) to estimate $\gamma_{vib}(V)$ at 300 K. This new analysis of γ_{vib} agrees with our previously determined $\gamma_{vib}(V)$ within uncertainty, but Equation (5.11) predicts a shallower slope than our original analysis (Section 4.2) (*Murphy et al.*, 2011b). Using the common parameterization $\gamma_{vib}(V) = \gamma_{vib,0}(V/V_0)^q$, where the subscript *0* corresponds to ambient pressure conditions and q determines the curvature of $\gamma_{vib}(V)$, we previously found a preferred q value range of 0.8 to 1.2 for $\gamma_{vib,0} = 2.0 \pm 0.1$ (Section 4.2) (*Murphy et al.*, 2011b); the determination using Equation (5.11) predicts $q \sim 0.4$ and a smaller $\gamma_{vib,0}$. Part of this discrepancy may arise from the volume independence of our $\alpha_{vib}K_T$, which significantly influences the volume dependence of γ_{vib}.

The two methods for determining $\gamma_{vib}(V)$ have better agreement at our larger compression points, with identical values at $V = 4.89 \pm 0.02$ cm^3/mol and 4.81 ± 0.02 cm^3/mol; at our largest compression point, $\gamma_{vib}(4.58 \pm 0.02$ cm^3/mol$) = 1.40 \pm 0.03$ from Equation (5.11) and including all reported uncertainties, and 1.34 ± 0.1 from our original analysis (Section 4.2) (*Murphy et al.*, 2011b). We note that the larger uncertainty from our original analysis reflects the range of q values included in the final reported fit to our individual γ_{vib} points, which were determined from the volume dependence of the total phonon DOS. In fact, the use of Equation (5.11) involves a more circuitous path from the phonon DOS to γ_{vib} that relies on a number of independent parameters, thus introducing more uncertainties in the analysis presented here than our original analysis.

5.6.3 Equilibrium Isotope Fractionation from *β*-factors

The β-factors for ε-Fe at each of our compression points are plotted in Figure 5.3a at 300 K, and as separate lines as a function of inverse temperature ($10^6/T^2$) for $T \geq 1000$ K in Figure 5.3b. Uncertainties in our determined β-factors are temperature-independent, so we plot single error bars for select compression points at T = 1100 K, which reflect the propagation of our measured uncertainties for $E_K(V,T)$. In Figure 5.3a, one can see that the β-factors for each compression point are fairly distinct at 300 K. However, by the moderate temperature of 1000 K ($10^6/T^2 = 1$ K^{-2}), β-factors for our smallest and largest compression points are indistinguishable within uncertainty, suggesting only a weak pressure dependence at the relevant temperature conditions (Figure 5.3b). Finally, by ~1200 K (~0.7 K^{-2}), it becomes unclear whether the β-factors at all compression points are positive or negative. We note that we are currently exploring methods for determining the same β-factors using ε-Fe's average force constant, which can be obtained from an analysis of the 3rd-order moment of $S(E)$, similar to the procedure presented in Section 5.2. The advantage of our forthcoming analysis is that it should reduce the uncertainties in the β-factors, potentially providing the required volume resolution to evaluate isotopic shifts from equilibrium processes involving solid iron above 1000 K.

It has been suggested that anharmonic effects are likely to be minor at the extreme compressions discussed here (*Polyakov*, 1998; 2009). However, it is possible that the quasi-harmonic model does not accurately describe the behavior of ε-Fe at these high temperatures and, in turn, phonon–phonon or phonon–electron interactions may play a non-negligible role under these conditions. We rely on the quasi-harmonic model largely because of the lack of sufficient data on the temperature dependence of ε-Fe's phonon DOS (Section 3.5), but unknown temperature effects further increase the uncertainty of our high-temperature β-factors.

A similar analysis was performed by *Polyakov* (2009), based on the previously published NRIXS dataset measured by *Mao et al.* (2001) up to 153 GPa. His results are identical to ours within uncertainty, but reflect the larger scatter that is present in the dataset measured by *Mao et al.* (2001) (Figure 5.2b). We note that the goal presented by *Polyakov* (2009) was to explain isotopic ratios of the mantle based on equilibrium partitioning between pure iron and iron-bearing lower-mantle phases. This application is roughly based on the theory that primary differentiation of the Earth (i.e., core segregation) was achieved via the formation and sinking of dense, iron-rich droplets (e.g., *Stevenson*, 1981). These droplets would have interacted with the surrounding silicate-rich mantle materials as they descended, resulting in element and isotope partitioning between silicate- and iron-rich phases over a range of depths (pressures) and temperatures. Therefore, comparison of β-factors for ε-Fe and coexisting solid phases at the appropriate *PT* conditions could, in theory, be used to predict the distribution of heavy iron isotopes that results from equilibrium processes. However, we note that such iron–silicate interactions during core formation would have occurred over a range of depths, including those corresponding to modern-day upper-mantle pressures. In addition, we emphasize that the values reported both here and by *Mao et al.* (2001) are for solid ε-Fe, whose β-factors are expected to differ significantly from those of liquid iron. Therefore, a relevant discussion of core-formation models from iron's β-factors would require an NRIXS study of liquid iron at high pressures, which would be extremely challenging for reasons similar to those discussed in the following section.

5.6.4 Comparison of ε-Fe's Sound Velocities with PREM

As previously discussed in Sections 1.2 and 5.1, the sound velocities of iron have been investigated over many decades using a variety of theoretical and experimental techniques. In Figure 5.8, we plot our measured compressional sound velocities (v_p) as a function of pressure, which we determine from our measured volumes and the Vinet EOS reported by *Dewaele et al.* (2006). We also plot previously reported values from NRIXS and inelastic x-ray scattering (IXS) experiments at 300 K in Figure 5.8, but we do not include sound velocities measured by shock-compression experiments since the corresponding experimental conditions involve simultaneous high pressures and temperatures. Similar to our discussion about our $v_D(\rho)$ in Section 5.5, the overall trend of our $v_p(P)$ agree fairly well with previously reported values from NRIXS, but our curve defines a new, tightly constrained pressure dependence up to 171 GPa. In addition, our largest compression point defines a curvature that lowers the trend with pressure compared to that presented by *Mao et al.* (2001) (Figure 5.8).

The two data points from the IXS measurements executed by *Antonangeli et al.* (2004) at 112 GPa reflect experimental probes of v_p in two different crystallographic directions. *Antonangeli et al.* (2004) prepared a DAC with nonhydrostatic conditions in the sample chamber in order to develop texture in their polycrystalline ε-Fe sample. They then rotated the DAC with respect to the beam to investigate v_p along crystallographic directions that were 50º and 90º from the c-axis in ε-Fe, based on texturing effects. Their reported values of $v_p(50º) = 9.9 \pm 0.2$ km/s and $v_p(90º) = 9.45 \pm 0.15$ km/s are based on fits of the linear region of the phonon dispersion curve.

To discuss the apparent discrepancy between our results and those of *Antonangeli et al.* (2004) that is evident in Figure 5.8, we begin by pointing out a few fundamental differences between the two experimental techniques. First, we note the very different energy ranges of phonons that were used to obtain the sound velocities: we fit the low-energy region of our phonon DOS measured at 106 GPa ($V = 5.00 \pm 0.02$ cm^3/mol) with 3.5 meV < E < 28.5 meV (Table 5.2), while *Antonangeli et al.* (2004) determined v_p from $E \geq 35$ meV at 112 GPa (see Figure 4 in reference). Given the limited energy range utilized by *Antonangeli et al.* (2004) in their fit of the linear low-energy region of the phonon dispersion curve, we argue that it is difficult to resolve their reported anisotropy of only 0.1 km/s beyond uncertainties. In particular, we note that our experiments are not sensitive to anisotropies of this magnitude, because NRIXS measures the projected phonon DOS and, in turn, an average sound velocity from nearly all crystallographic directions (*Sturhahn*, 2000). As a result, direct comparison with IXS experiments—which are much more sensitive to crystal orientation because they select for longitudinal acoustic phonons—is not straightforward.

The most direct comparison would be between NRIXS sound velocities and an average v_p from IXS experiments performed over a wide range of crystallographic directions, which would require weeks of experiments. An alternative method is to apply values for the elastic stiffness constants of ε-Fe to the Christoffel equation (*Musgrave*, 1970) in order to determine the sound velocities for all crystallographic directions. Then, by using the proper averaging procedure (*Sturhahn*, 2000; *Sturhahn and Jackson*, 2007), we can explore how sensitive sound velocities determined with NRIXS are to crystallographic anisotropies. The elastic stiffness constants have not been measured because a single-crystal of ε-Fe does not yet exist, so we use values from first-principles calculations at 52 GPa and 300 K by *Steinle-Neumann et al.* (2004) in our calculations. We find v_p(0º) is only ~1% (< 100 km/s) faster than v_p(90º)—where 0º corresponds to a wave propagating along the c-axis direction—which agrees qualitatively with the orientation dependence of the anisotropy reported by *Antonangeli et al.* (2004). However, the predicted magnitude of anisotropy is significantly smaller and would not be detectable with NRIXS, based on the uncertainties of our high-statistical quality dataset. In particular, if we apply the proper averaging procedures, we find that v_p(50 GPa) from NRIXS is ~10 km/s faster than v_p(90º), and ~70 km/s slower than v_p(0º), both of which lie within our reported uncertainties at ~50 GPa. We note that this argument is meant to be qualitative because there is a large amount of uncertainty associated with the elastic stiffness constants of ε-Fe, which are the primary input parameters for this calculation.

Next, to compare our results with seismic observations, we plot in Figure 5.9 our $v_p(\rho)$ and $v_s(\rho)$ with those predicted for the liquid outer core (~136 to 329 GPa) and solid inner core (P ~ 329 to 364 GPa) by the preliminary reference Earth model (PREM) (*Dziewonski and Anderson*, 1981). For a qualitative comparison—since our experiments were performed at 300 K and the temperature at Earth's inner core boundary (ICB) is thought to be between ~5000 and 7000 K based on previous reports of the melting behavior

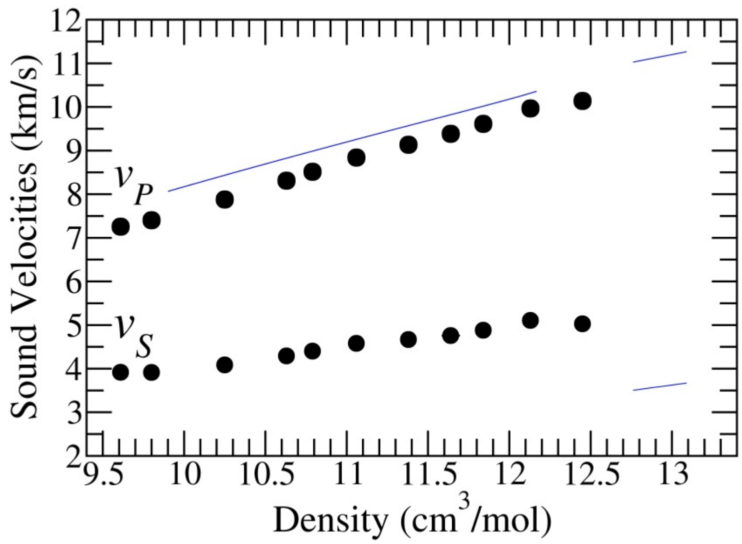

Figure 5.9. Density dependence of our compressional and shear sound velocities of ε-Fe at 300 K with PREM. Black circles give our compressional and shear sound velocities as a function of density, $v_p(\rho)$ and $v_s(\rho)$; blue lines show PREM throughout Earth's core (*Dziewonski and Anderson*, 1981). We note that $v_s = 0$ in Earth's liquid outer core, and the apparent discontinuity in PREM corresponds to the density jump across the ICB.

of ε-Fe (Section 1.2)—we use a linear fit of our data (i.e., Birch's Law) to extrapolate our $v_p(\rho)$ to the expected density of the ICB (*Birch*, 1960; 1961). From an errors-weighted least-squares linear fit of our $v_p(\rho)$, we find a slope of 1.07 ± 0.04, which predicts v_p(330 GPa, 300 K) for ε-Fe is ~9% larger than the reported value from PREM on the inner core side of the ICB, where the corresponding density of ε-^{57}Fe is 14.1 g/cm^3 (*Dewaele et al.*, 2006). Birch's law is only strictly relevant for compressional sound velocities, but in the absence of reliable information about the density dependence of ε-Fe's shear modulus beyond our compression range, we use the same relationship to estimate v_s(330 GPa, 300 K) ~67% larger than the reported value for PREM at a density for ε-^{57}Fe of 14.1 g/cm^3.

It is possible to probe the high-*PT* sound velocities of ε-Fe with NRIXS, and results from such experiments were previously reported by *Shen et al.* (2004) at 20 and 29 GPa up to 720 K using resistive heating methods; and by *Lin et al.* (2005) between 39 and 73 GPa and up to 1700 K using laser heating methods. However, as previously discussed (Section 3.5), these studies did not collect either ambient- or high-temperature *in situ* XRD, so their reported pressures are based on ruby fluorescence measurements collected before and after heating. In addition, only *Lin et al.* (2005) considered thermal pressure effects via an existing thermal EOS (*Dubrovinsky et al.*, 1998). Additional experiments are needed at higher-*PT* conditions—with higher statistical quality and *in situ* XRD—in order to better constrain the sound velocities of ε-Fe at Earth's core conditions. However, the *PT* conditions that are currently feasible for NRIXS experiments are well below those expected for Earth's core, and are limited by the need for very stable temperatures over timescales of several hours (*Sturhahn and Jackson*, 2007; *Gao et al.*, 2009).

Finally, it is thought that the Earth's core comprises an iron-nickel alloy that incorporates some light elements (e.g., *McDonough*, 2003). Now that the compressional and shear sound velocities of pure iron have been firmly established up to an outer core pressure of 171 GPa, an important next step is to investigate the effects of alloying light elements with iron on its thermoelastic properties. A number of studies have been dedicated to probing the sound velocities of iron alloys, and a comparison with their existing results will be one of the primary focuses of Chapter 6.

Chapter 6

Discussion and Conclusions

6.1 Introduction

Now that we have firmly established the vibrational properties of ε-Fe, we will devote this chapter to discussing what conclusions we can draw about the Earth's core, which is composed primarily of iron. Many of the parameters presented in the preceding chapters were obtained from the integrated total phonon density of states (DOS), including the Lamb-Mössbauer factor and vibrational components of the free energy, internal energy, kinetic energy, specific heat capacity, and entropy. In turn, the properties of ε-Fe that were derived from these parameters—e.g., thermal pressure, melting behavior, Grüneisen parameter, reduced equilibrium isotopic partition function ratios, and thermal expansion coefficient—also depend on knowledge of the total phonon DOS. Since nuclear resonant inelastic x-ray scattering (NRIXS) is an isotope-selective technique that only probes the phonons experienced by the resonant nuclei in the lattice (^{57}Fe), investigations of iron alloys with NRIXS results in a partial projected phonon DOS (*Sturhahn*, 2000). Therefore, analysis of the effects of alloying on the thermodynamic properties of iron using NRIXS alone is somewhat indirect at this time. An exciting possibility for future studies is the combination of NRIXS measurements with density-functional theory (DFT) calculations. In particular, for DFT calculations of an iron alloy, one can separately determine phonons experienced by iron, and phonons experienced by the alloy components (many of which are also experienced by ^{57}Fe). The consistency between the two techniques could then be confirmed via comparison between the calculated partial phonon DOS and that measured by NRIXS.

In the meantime, we will devote the next two sections to discussing the effects of alloying and temperature on the sound velocities of ε-Fe, in an effort to better constrain the composition of the core via comparison with seismic observations (e.g., *Dziewonski and Anderson*, 1981; *Kennett et al.*, 1995). It has been shown previously that the low-energy region of the phonon DOS provides the Debye sound velocity of the bulk sample (e.g., *Hu et al.*, 2003), so we can investigate the effects of alloying on iron's sound velocities by comparing our results with those determined from NRIXS and inelastic x-ray scattering (IXS) experiments on iron alloys (Section 6.2). We note that the following sections do not include comparisons with results from theoretical calculations (e.g., *Stixrude et al.*, 1997; *Steinle-Neumann et al.*, 2001; *Vočadlo et al.*, 2009) or shock-compression experiments (e.g., *Jeanloz*, 1979; *Brown and McQueen*, 1986; *Nguyen and Holmes*, 2004; *Huang et al.*, 2011) on the high-*PT* sound velocities of either iron or iron alloys. In addition, we do not consider results from other static-compression techniques are also capable of investigating high-pressure sound velocities, such as brillouin spectroscopy (BS), impulsive stimulated light scattering (ISLS), and ultrasonics. For opaque samples, BS only excites scattering from surface acoustic modes, whose relationship to bulk acoustic modes is not well-known (e.g., *Crowhurst et al.*, 1999). In addition, ISLS and BS require accurate knowledge of the sample surface, which is very difficult to achieve at core pressures (e.g., *Crowhurst et al.*, 2004). Finally, data from BS and ultrasonics have largely been restricted to lower pressures than those probed by NRIXS and IXS because of experimental geometries and low signal to noise ratios at large compressions (e.g., *Mao et al.*, 1999).

In Section 6.3, we investigate the effects of temperature on ε-Fe's sound velocities and density using a finite-strain model, and we conclude with a summary of the major findings of this thesis (Section 6.4).

6.2 Alloying Effects

As previously discussed in Section 1.2, the Earth's core is thought to contain ~5 to 10 wt% nickel (Ni) and some light elements (*McDonough*, 2003), based on the comparison of seismic and cosmochemical observations with experiments. Commonly cited candidate light elements for the core include hydrogen (H), carbon (C), oxygen (O), silicon (Si), and sulfur (S). The focus of this section will be on evaluating the current understanding of the effects of alloying Ni and select light elements (H, C, Si, and S) with iron on its high-pressure thermoelastic properties, based on NRIXS and IXS experiments. We note that *Struzhkin et al.* (2001) investigated FeO in the diamond-anvil cell with NRIXS, but they reported only a calculated curve for the sound velocities as a function of momentum transfer, without any discrete data points (see Figure 4b in reference). In addition, previous IXS measurements of FeO by *Badro et al.* (2007) report v_p only as a function of density, without a clear explanation of the pressure range, crystal structure, or XRD measurements used to determine the relevant amount of compression. Therefore, analysis of the effect of alloying oxygen with Fe is not straightforward and will not be included here.

To facilitate comparison of our measured sound velocities for ε-Fe with results from existing experiments on iron alloys, we begin by converting our measured volumes (densities) to pressures using the Vinet equation of state (EOS) parameters reported by *Dewaele et al.* (2006) (Tables 2.1 and 2.2). We then plot in Figure 6.1 the *pressure* dependence of our measured Debye sound velocities (v_D; filled circles) with those reported from previous NRIXS studies (*Lin et al.*, 2003c; *Lin et al.*, 2004; *Mao et al.*, 2004; *Gao et al.*, 2009). One of the most striking features of Figure 6.1 is the limited pressure range over which the sound velocities of iron alloys have been probed with NRIXS. A number of the data points lie at pressures below that of the α→ε (bcc→hcp) transition of pure iron, and thus cannot be directly compared with our results. Data collection times are likely responsible, in part, for the sparse data coverage on the sound velocities of iron alloys, since a single high-pressure IXS or NRIXS measurement can take days to collect due to low counting rates at larger compressions (i.e., thinning of the sample). Therefore, it is likely that the compression range over which the sound velocities of iron alloys have been measured will expand with time, as more data are collected. One possible approach for maximizing counting rates and, in turn, performing higher-pressure experiments, is to apply the previously discussed boron-epoxy insert, whose high shear strength helps to maintain a thick sample and stabilize the gasket (Section 2.1.2).

In the following subsections, we plot only the pressure range over which our data overlap with existing data for the compressional and shear sound velocities of iron alloys. Thus, Figures 6.2–6.5 provide a better depiction of the relevant features that will be discussed in Sections 6.2.1 and 6.2.2. In addition, we perform a quantitative analysis of how our v_p and v_s for ε-Fe compare with those reported for iron alloys. Finally, we evaluate whether existing data for iron alloys can provide any trends in how the alloying of light

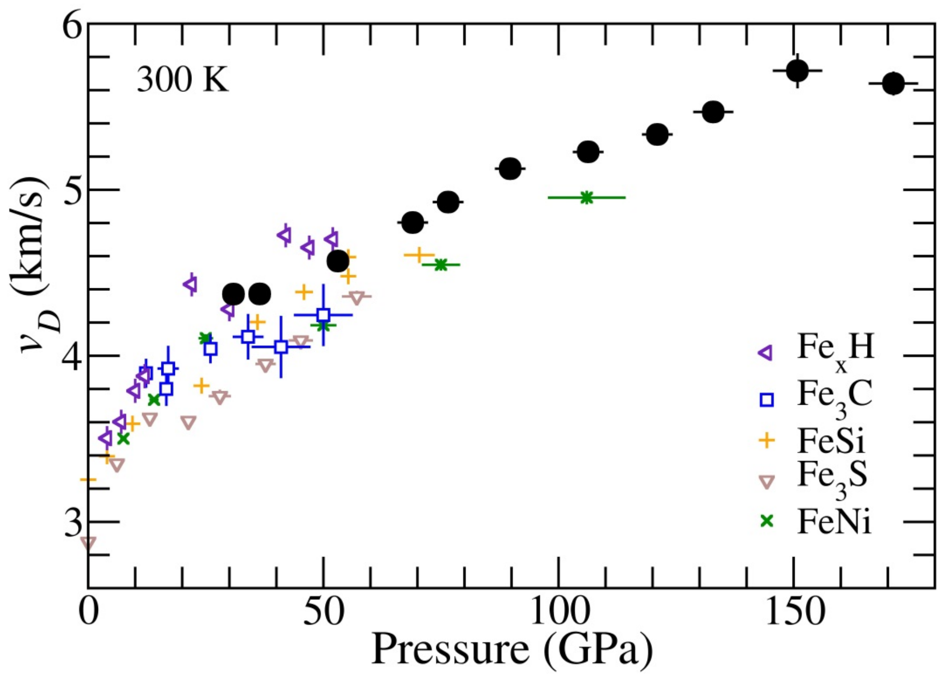

Figure 6.1. Debye sound velocities of ε-Fe and iron alloys. Black circles give our measured Debye sound velocities (v_D) for ε-Fe as a function of pressure, which is determined from our *in situ* XRD and the Vinet EOS parameters reported by *Dewaele et al.* (2006). The remaining symbols give $v_D(P)$ from NRIXS experiments on FeH_x (purple left triangle; (*Mao et al.*, 2004)); Fe_3C (dark blue square; (*Gao et al.*, 2009)); $Fe_{0.85}Si_{0.15}$ (orange cross; (*Lin et al.*, 2003c)); Fe_3S (brown downward triangle; (*Lin et al.*, 2004)); and $Fe_{0.92}Ni_{0.08}$ (green x; (*Lin et al.*, 2003c)). For Figures 6.2–6.5, we note that we plot only the compression range over which our data overlap with existing data for iron alloys.

elements affects the sound velocities of iron and, thus, help to better constrain the composition of Earth's core via a comparison with seismic observations.

6.2.1 Alloying Effects on Compressional Sound Velocities

In Figure 6.2, we plot the pressure dependence of our compressional sound velocities (v_p; filled circles) with those from NRIXS (empty squares) and IXS (empty triangles) studies of iron alloys (*Lin et al.*, 2003c; *Lin et al.*, 2004; *Mao et al.*, 2004; *Kantor et al.*, 2007; *Fiquet et al.*, 2009; *Gao et al.*, 2009; *Antonangeli et al.*, 2010; *Shibazaki et al.*, 2012). The limited compression range over which the compressional sound velocities of iron alloys have been probed with NRIXS or IXS is demonstrated by the restricted pressure range that is plotted in Figure 6.2 (compared to Figure 6.1). A new trend that is evident in Figure 6.2 is the often significant disagreement between reported values for v_p from IXS and NRIXS experiments on a similar iron alloy, the scatter from which increases the overall uncertainty for that composition. One likely explanation for the disagreement between sound velocities measured with NRIXS and IXS is the fact that they are based on

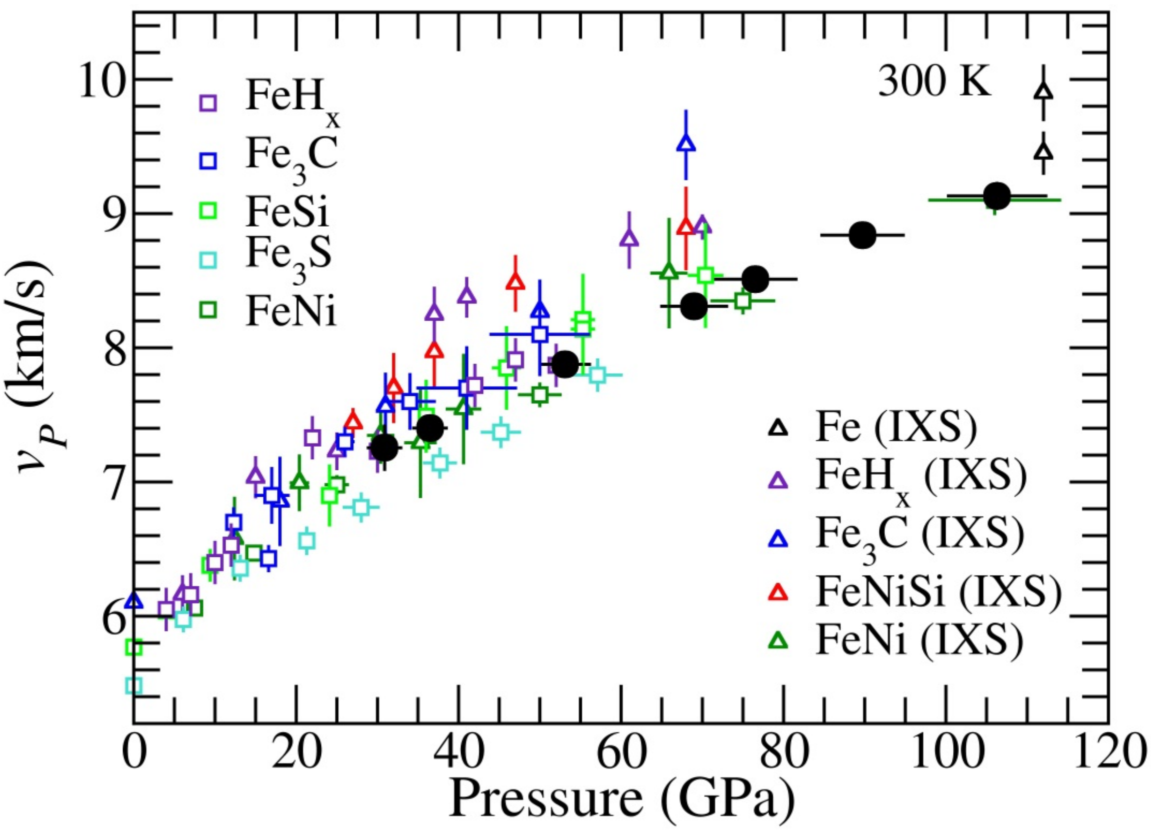

Figure 6.2. Compressional sound velocities of ε-Fe and iron alloys. Black circles give our measured compressional sound velocities (v_p) for ε-Fe as a function of pressure, which is determined from our *in situ* XRD and the Vinet EOS parameters reported by *Dewaele et al.* (2006). We note that we only plot our $v_p(P)$ at pressures that overlap with reported values for the following iron alloys. Unfilled squares give $v_p(P)$ from NRIXS experiments on FeH_x (purple; (*Mao et al.*, 2004)); Fe_3C (dark blue; (*Gao et al.*, 2009)); $Fe_{0.85}Si_{0.15}$ (light green; (*Lin et al.*, 2003c)); Fe_3S (cyan; (*Lin et al.*, 2004)); and $Fe_{0.92}Ni_{0.08}$ (dark green; (*Lin et al.*, 2003c)). Unfilled triangles give $v_p(P)$ from IXS experiments on Fe (black; (*Antonangeli et al.*, 2004)); FeH_x (purple; (*Shibazaki et al.*, 2012)); Fe_3C (dark blue; (*Fiquet et al.*, 2009)); $Fe_{0.89}Ni_{0.04}Si_{0.07}$ (red; (*Antonangeli et al.*, 2010)); and $Fe_{0.78}Ni_{0.22}$ (green; (*Kantor et al.*, 2007)).

very different energy ranges (see Section 5.6.4). For example, *Lin et al.* (2003c) determined v_p for $Fe_{0.92}Si_{0.08}$ (in weight %) by fitting the low-energy region of their measured phonon DOS (from NRIXS) with 3.5 meV < E < 14 meV, while *Antonangeli et al.* (2010) obtained v_p for $Fe_{0.89}Ni_{0.04}Si_{0.07}$ (in weight %) from a linear fit of their IXS data with $E \geq 15$ meV.

Similar discrepancies between sound velocities measured with NRIXS and IXS are evident in the data for double hexagonal close-packed (dhcp) FeH_x (Figure 6.2): *Mao et al.* (2004) report $v_p(P)$ from NRIXS measurements of dhpc-FeH_x that are identical to our results for ε-Fe up to 52 GPa, while *Shibazaki et al.* (2012) report $v_p(P)$ from IXS measurements up to 70 GPa that are well above our values for ε-Fe and have a very different slope. In addition to the very different energies used to obtain these sound velocities, another possible contributing factor to this discrepancy is the difficulty associated with determining the exact amount of hydrogen that enters the lattice, as denoted by the subscript "X." This challenge is somewhat unique to hydrogen-bearing alloys, because hydrogen is not directly detectable with XRD, and it cannot be measured in recovered samples because the very small hydrogen atoms can escape the lattice upon decompression to ambient pressures. As a result, both *Mao et al.* (2004) and *Shibazaki et al.* (2012) estimate the amount of hydrogen in their samples to correspond to x $\approx$ 1, based on comparisons with existing equations of state (EOS) for the dhcp crystal structure of FeH (*Badding et al.*, 1991; *Hirao et al.*, 2004a).

Another noticeable feature from Figure 6.2 is that the reported uncertainties for the sound velocities of iron alloys are often relatively large, even at small compressions. For example, reported errors for IXS measurements of the compressional sound velocities of $Fe_{0.89}Ni_{0.04}Si_{0.07}$ at pressures that overlap with our experimental compression range (32 to

68 GPa) are on the order of 200 to 300 m/s (*Antonangeli et al.*, 2010); errors reported for the compressional sound velocities of $Fe_{0.92}Si_{0.08}$ measured by NRIXS over a similar pressure range (36 to 55 GPa) are between 300 and 400 m/s (*Lin et al.*, 2003c). Errors of this magnitude only correspond to a few percent of the measured v_p, but it is important to note that they are from measurements performed at pressures that are ~1/2 that of Earth's core–mantle boundary. Not only are experimental uncertainties likely to increase with compression as counting rates decrease and statistical fluctuations become increasingly important, but extrapolation of NRIXS and IXS data to core pressures will only exacerbate the existing divergence between them at lower pressures. In addition, the amount of light elements present in the core is thought to be only a few percent (e.g., *Badro et al.*, 2007; *Sakai et al.*, 2011), so it is essential to have sound velocity data of similarly high statistical quality as our measurements (Table 5.2) in order to first compare with pure iron and, thus, better constrain the identity and amounts of light elements that are present in the core.

In addition to the magnitude of reported uncertainties for the compressional sound velocities in Figure 6.2, it is important to consider how they were calculated from the corresponding experimental data. For example, *Lin et al.* (2004) report $v_p(P)$ from NRIXS measurements of the tetragonal phase of Fe_3S that have uncertainties on the order of 1.5%. However, *Lin et al.* (2004) did not measure *in situ* XRD, so their reported pressures are based on fluorescence measurements of ruby chips in the sample chamber and the nonhydrostatic ruby pressure scale reported by *Mao et al.* (1978). Their sound velocities are then based on the pressures determined from these secondary pressure markers, which are used with an established EOS (e.g., *Fei et al.*, 2000) to determine the sample's density in the absence of *in situ* XRD and, in turn, obtain sound velocities from the phonon DOS. It

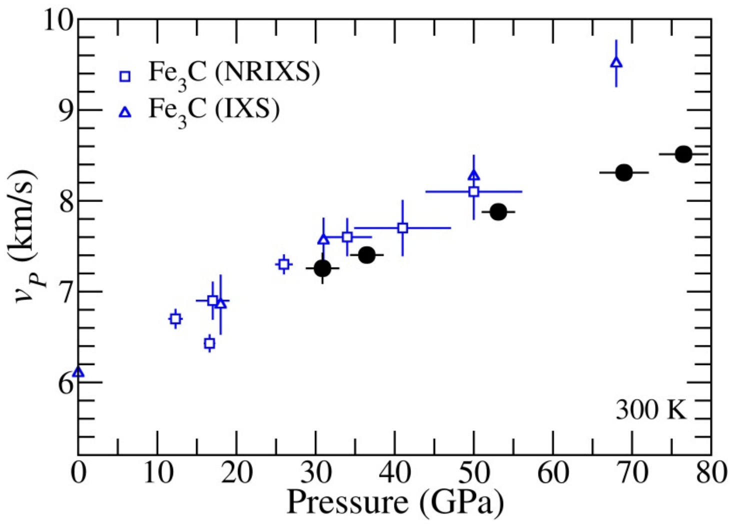

Figure 6.3. Compressional sound velocities of ε-Fe and Fe_3C. Black circles give our measured compressional sound velocities (v_p) for ε-Fe as a function of pressure. Blue symbols give $v_p(P)$ for Fe_3C from NRIXS (squares (*Gao et al.*, 2009)) and IXS (triangles; (*Fiquet et al.*, 2009)).

is important to note that uncertainties in pressure propagate to those of sound velocities, so an underestimation of pressure uncertainties can result in artificially low sound velocity errors, particularly if the reported EOS parameter uncertainties are not considered. Therefore, we reemphasize the importance of measuring *in situ* XRD, which provides direct knowledge of the sample density and, in turn, increasingly accurate sound velocities.

Finally, *Gao et al.* (2009) and *Fiquet et al.* (2009) did measure *in situ* XRD along with NRIXS and IXS, respectively, so we are able to provide a more detailed comparison between their results and ours for ε-Fe (Figure 6.3). Both studies investigated orthorhombic Fe_3C; *Gao et al*. (2009) performed NRIXS and *in situ* XRD experiments up to 50 GPa, and *Fiquet et al.* (2009) performed IXS and *in situ* XRD experiments up to 68 GPa. The three largest compression points from each of these studies overlap with our experimental pressure range. *Gao et al.* (2009) reported compressional sound velocities that are ~2.5% larger than ours for ε-Fe at similar pressures (Table 5.2), which is within their reported uncertainties for those compression points. In addition, two of the sound velocities measured by *Fiquet et al.* (2009) agree well with those measured by *Gao et al.* (2009), and are ~4% to 5% larger than our measured sound velocities at similar pressures. However, v_p at the largest compression point measured by *Fiquet et al.* (2009) (P = 68 GPa) is ~15% larger than our measured sound velocity at 69 GPa. The cause of this sudden increase in v_p measured by *Fiquet et al.* (2009) is not immediately clear, since measurements by *Gao et al.* (2009) do not show any indication of a positive curvature up to their largest compression point at 50 GPa, and existing EOS experiments on orthorhombic Fe_3C observed no phase transitions up to 73 GPa.

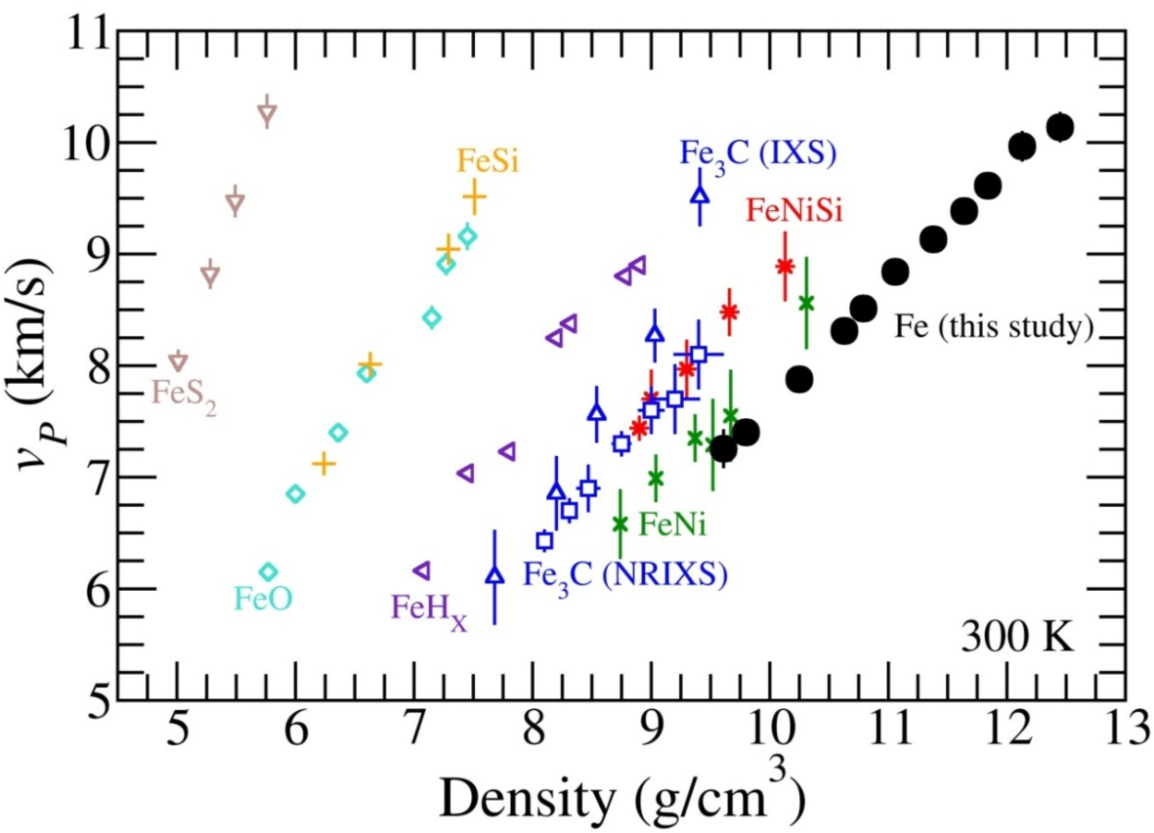

Figure 6.4. Density dependence of compressional sound velocities of ε-Fe and iron alloys. Black circles give our measured compressional sound velocities (v_p) for ε-Fe as a function of density, which is determined from our *in situ* XRD and m = 56.95 g/mol for 95% isotopically enriched ^{57}Fe. Blue symbols give $v_p(\rho)$ for Fe_3C from NRIXS (squares (*Gao et al.*, 2009)) and IXS (triangles; (*Fiquet et al.*, 2009)). All other symbols are labeled on the figure and are from IXS measurements by *Badro et al.* (2007) (FeS_2, brown downwards triangle; FeSi, orange cross; FeO, turquoise diamond); *Kantor et al.* (2007) ($Fe_{0.78}Ni_{0.22}$, green x); *Antonangeli et al.* ($Fe_{0.89}Ni_{0.04}Si_{0.07}$, red star); and *Shibazaki et al.* (2012) (FeH_x, purple left-triangle).

Because both studies also measured *in situ* XRD, we can further investigate this discrepancy via the density dependence of their compressional sound velocities for Fe_3C (Figure 6.4). In particular, we compare the slopes of $v_p(\rho)$ measured by each study: the data measured by *Fiquet et al.* (2009) suggest a slope of 1.90 ± 0.23 (km/s)/(g/cm^3) for $v_p(\rho)$, while values reported by *Gao et al.* (2009) correspond to a slope of 1.29 ± 0.14 (km/s)/(g/cm^3). For comparison, we note that our $v_p(\rho)$ for ε-Fe reveal a slope of 1.07 ± 0.04 (km/sec)/(g/cm^3) (Section 5.6.4). The disagreement between the slopes measured by *Fiquet et al.* (2009) and *Gao et al.* (2009) is beyond the relevant uncertainties, which are based on an errors-weighted least-squares linear fit of the reported $v_p(\rho)$ from each study. We note that the largest compression point measured by *Fiquet et al.* (2009) deviates from the linear trend that is suggested by their four smallest compression points. Inspection of their data (see Figure 2 in reference) reveals that *Fiquet et al.* (2009) determined v_p from a minimum momentum transfer of 4 nm^{-1} and $E \geq 20$ meV for their first four compression points, but from a minimum momentum transfer of 6 nm^{-1} and $E \geq 35$ meV at 68 GPa. For comparison, we note that *Gao et al.* (2009) determined v_p by fitting the low-energy region of their measured phonon DOS with 3 meV < E < 12 meV. Therefore, the limited energy range of the fit by *Fiquet et al.* (2009) for their final compression point could be responsible for the disagreement between their results and those of *Gao et al.* (2009).

Also in Figure 6.4, we plot reported results for the density dependence of v_p from additional IXS studies that measured *in situ* XRD (*Badro et al.*, 2007; *Kantor et al.*, 2007; *Antonangeli et al.*, 2010; *Shibazaki et al.*, 2012). The apparently linear dependence of v_p with respect to density for most data sets (i.e., compositions) is consistent with Birch's Law (*Birch*, 1960; 1961). We note that *Badro et al.* (2007) do not report corresponding pressures, crystal structures, or EOS for their measured densities of Fe_3C, FeO, FeSi, FeS, and FeS_2, which inhibits direct comparison with our results for ε-Fe at the same pressure (i.e., depth in the Earth). In addition, we point out that for both NRIXS and IXS investigations of Fe-Ni alloys (Figures 6.1 and 6.2), Ni has been shown to have only a slight effect on the compressional sound velocities of pure iron, for both hcp (*Mao et al.*, 1990; *Lin et al.*, 2003c) and fcc (*Kantor et al.*, 2007) crystal structures.

In summary, we have evaluated the effects of alloying on iron's compressional sound velocities by comparing our measured $v_p(\rho)$ and $v_p(P)$ with those reported for iron alloys containing Ni and candidate light elements for the core (H, C, Si, S). In theory, it should be possible to combine our measured densities and sound velocities with those reported for iron alloys, and invert the resulting dataset to better constrain the composition of Earth's core via comparison with seismic observations. However, a higher statistical quality, larger compression range, and better understanding of discrepancies from different experimental techniques that have been used to probe the compressional sound velocities of iron alloys are necessary before such an inversion will be feasible. In addition, temperature effects must be considered in order to make direct comparisons with seismic observations of Earth's core (Section 6.3).

6.2.2 Alloying Effects on Shear Sound Velocities

We begin our discussion of the effects of alloying on the shear velocities of ε-Fe by recalling that our measured shear sound velocities for ε-Fe are estimated to be ~67% larger than those predicted by PREM on the inner core side of the inner–core boundary (ICB; Section 5.6.4) (*Dziewonski and Anderson*, 1981). This estimate is based on a linear fit and extrapolation of our $v_s(\rho)$ to the predicted density of ε-Fe at the depth of the ICB and at

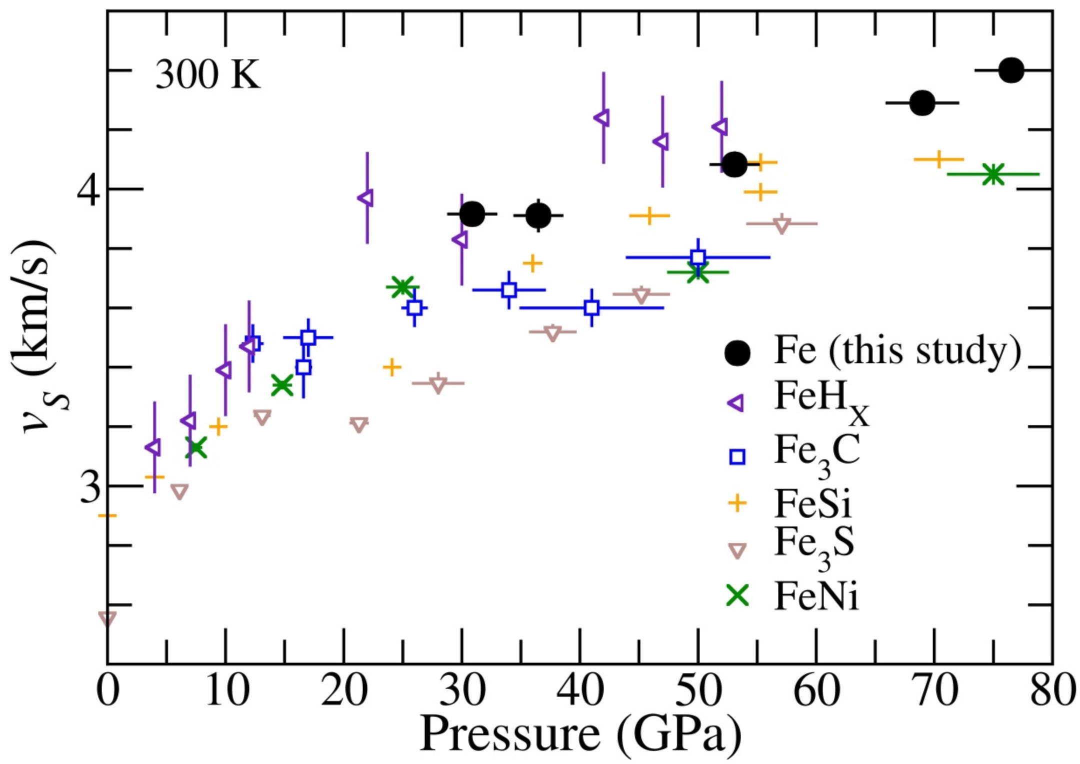

Figure 6.5. Shear sound velocities of ε-Fe and iron alloys. Black circles give our measured shear sound velocities (v_s) for ε-Fe as a function of pressure, which is determined from our *in situ* XRD and the Vinet EOS parameters reported by *Dewaele et al.* (2006). The remaining symbols give $v_s(P)$ from NRIXS experiments on FeH_x (purple left triangle; (*Mao et al.*, 2004)); Fe_3C (dark blue square; (*Gao et al.*, 2009)); $Fe_{0.85}Si_{0.15}$ (orange cross; (*Lin et al.*, 2003c)); Fe_3S (brown downward triangle; (*Lin et al.*, 2004)); and $Fe_{0.92}Ni_{0.08}$ (green x; (*Lin et al.*, 2003c)).

300 K (*Dewaele et al.*, 2006), which revealed a slope of 0.44 ± 0.02 (km/s)/(g/cm^3).

In Figure 6.5, we plot the pressure dependence of our measured shear sound velocities (v_s; filled circles) with those reported from previous NRIXS studies (*Lin et al.*, 2003c; *Lin et al.*, 2004; *Mao et al.*, 2004; *Gao et al.*, 2009). The first noticeable feature when qualitatively comparing existing measurements of the high-pressure v_p (Figure 6.2) and v_s (Figure 6.5) for iron alloys is that far fewer data points have been measured for the latter quantity. This is a result of the fact that the IXS studies included in Figures 6.2–6.4 were performed on polycrystalline samples, in which the signal to noise ratio is too low to detect the shear mode and, in turn, the shear sound velocities of iron alloys.

As before, it is immediately obvious that experiments must be performed over a wider pressure range in order to make reasonable inferences about the corresponding sound velocities in Earth's core, either via comparison with average Earth models or with the sound velocities of ε-Fe (Figure 6.5). A maximum of four data points for an iron alloy containing a given candidate light element (i.e., H, C, Si, or S) overlap with our experimental compression range, and the largest compression point plotted in Figure 6.5 is at 70 GPa. We note that the shear sound velocities of hcp-$Fe_{0.92}Ni_{0.08}$ have been measured with NRIXS up to 106 GPa (*Lin et al.*, 2003c), and that they are ~7% smaller than those of ε-Fe, based on an average of the three overlapping compression points. However, there is a large amount of scatter in the dataset presented by *Lin et al.* (2003c), thus prohibiting a more quantitative treatment. In general, we conclude that while Ni may not have a strong influence on the density or compressional sound velocities of pure iron, its effects on the shear sound velocities (i.e., the shear moduli) could be significant.

Another striking feature in Figure 6.5 is that the shear sound velocities of dhcp-FeH_x are slightly larger than—but identical within uncertainty to—those of ε-Fe. We note that this is opposite of the trend desired to move closer to matching seismic observations (independent of temperature effects). In addition, 15 atomic% Si appears to have little effect on the shear sound velocities of ε-Fe up to 55 GPa (*Lin et al.*, 2003c), while the shear sound velocity reported for their largest compression point (70 ± 3 GPa) is ~4.5% smaller than our measured v_s(69 ± 4 GPa). Using the EOS for hcp-$Fe_{0.85}Si_{0.15}$ reported by *Lin et al.* (2003a), we find ρ(55 GPa) ~ 9.8 g/cm^3 and ρ(70 GPa) ~ 10.1 g/cm^3, correcting for the mass of 95% isotopically enriched ^{57}Fe. Together with their reported v_s(55 GPa) = 4.09 ±

0.02 km/s and v_s(70 GPa) = 4.10 ± 0.02 km/s, the predicted increase in shear modulus (μ) between 55 and 70 GPa is expected to be only ~6.7 ± 2.4 GPa (4.5%), following $v_s^2 = \mu/\rho$ and considering reported uncertainties in v_s. For comparison, we note that the increase in μ between compression points at 46 and 55 GPa is 17 GPa (12%), indicating a significantly different trend immediately before their largest compression point. Additional measurements at compression points beyond 70 GPa are needed to determine whether the largest compression point measured by *Lin et al.* (2003c) defines a noticeably different slope of $v_s(P)$ or a new lower trend in v_s, or whether it requires a different explanation.

A similar discussion applies to reported values for the shear sound velocities of orthorhombic Fe_3C, which were measured by *Gao et al.* (2009) up to 50 GPa (Figure 6.5). It is possible that the small dip in shear sound velocity at 41 GPa corresponds to a softening in v_s at that pressures, but with only a single larger compression data point, it is difficult to determine whether a new lower trend in $v_s(P)$ is being defined for Fe_3C, or perhaps that its slope is significantly shallower than that of ε-Fe. *Gao et al.* (2009) report that their compressional sound velocities at pressures above the magnetic collapse between 4.3 and 6.5 GPa increase linearly with density, i.e., they do not report a softening in v_s. In particular, they find a slope of $v_s(\rho)$ to be ~0.24 (km/s)/(g/cm^3), compared to our reported value of 0.44 ± 0.02 (km/s)/ (g/cm^3) for ε-Fe.

Finally, Figure 6.5 shows a trend of $v_s(P)$ for tetragonal Fe_3S that is distinctly lower than that of ε-Fe, but with a similar slope. In particular, shear sound velocities for Fe_3S reported by *Lin et al.* (2004) are ~8% smaller on average than those of ε-Fe at similar pressures. A larger compression range would be useful for determining an accurate slope for $v_s(P)$ of Fe_3S and, in turn, whether $v_s(P)$ of Fe_3S and ε-Fe remain roughly parallel or ultimately cross at a higher pressure. We reemphasize here our discussion in Section 6.2.1 about additional uncertainties associated with determining sound velocities from densities based on secondary pressure markers and an existing EOS, rather than *in situ* XRD.

In summary, we have investigated the effects of alloying on iron's shear sound velocities by comparing our measured $v_s(\rho)$ and $v_s(P)$ with those reported from NRIXS studies of iron alloys. With the exception of H, we found that the alloying of all other candidate light elements (C, Si, and S) presented in this chapter results in lower shear sound velocities than those measured for ε-Fe. However, as we concluded in the previous subsection, the large scatter and limited compression range of available experimental data on the shear sound velocities of iron alloys do not allow for a quality inversion in order to better constrain the composition of Earth's core via comparison with seismic models.

6.3 Temperature Effects

In order to directly compare experimental values for the sound velocities of candidate core compositions with seismic observations, the effects of temperature must be considered. In particular, all of the experimental results presented in the previous sections were measured at 300 K, while temperatures in Earth's core are on the order of thousands of Kelvin (Section 1.2). However, due to experimental challenges for NRIXS (and IXS) at simultaneous high pressure and temperature (*PT*) conditions (Section 5.6.4), little is known about the temperature effects on the phonon DOS (dispersion of acoustic phonons) of ε-Fe and, in turn, its sound velocities. Available information from NRIXS experiments on ε-Fe comes from two previously discussed high-*PT* studies by *Shen et al.* (2004) and *Lin et al.* (2005) (Section 5.6.4). Both studies found that ε-Fe's sound velocities decrease with increasing temperature, and *Lin et al.* (2005) reported the following values for the temperature derivatives of v_p, v_s, and the shear modulus (μ) at a constant density of 10.25 g/cm^3 (determined from secondary pressure markers and an EOS): $dv_p/dT \approx$ -0.35 m/s/K; $dv_s/dT \approx$ -0.46 m/s/K; and $d\mu/dT \approx$ -0.035 GPa/K. However, the limited compression range, lack of *in situ* XRD, and large scatter and uncertainties—in addition to inherent challenges associated with maintaining stable temperatures over timescales of many hours—make overall trends difficult to quantify.

Here we approximate the effects of temperature on our measured sound velocities for ε-Fe using a model based on finite-strain theory that was originally presented by *Duffy and Anderson* (1989). In general, we will determine the structural and thermoelastic properties of ε-Fe at an anchor point (i.e., one of our compression points after accounting for temperature effects), and then use finite-strain theory to extrapolate those properties along an adiabat to the pressures of Earth's solid inner core. More specifically, we begin by determining the density (ρ) of ε-Fe at the temperature of our anchor point from our measured density at 300 K and an assigned value for its thermal expansion coefficient (α). Then, using the temperature dependence of the density and assigned values for ε-Fe's ambient-temperature elastic moduli (K, μ) and their pressure (K', μ') and temperature ($\partial K/\partial T$ and $\partial \mu/\partial T$) derivatives, we calculate values for the elastic moduli at the temperature of our anchor point. Finally, we extrapolate the high-*PT* density and elastic moduli to greater depths along an adiabat using finite-strain theory (*Duffy and Anderson*, 1989), in order to allow for comparison between the structural and thermoelastic properties of ε-Fe at high-*PT* conditions and those of the solid inner core.

To investigate whether finite-strain theory accurately describes the density dependence of our measured compressional and shear sound velocities, we build a simple finite-strain model that is anchored at the density (pressure) of our smallest compression point, so that many of the necessary input parameters can be taken either directly from our data (ρ, α), or from a combination of our data and the Vinet EOS parameters reported by *Dewaele et al.* (2006) (K_S, K_S', μ, μ'). Specific values assigned for each necessary input parameter are given in Table 6.1. We set the temperature at the foot of the adiabat to be 300 K to remove all temperature effects, which are calculated relative to the ambient temperature conditions at which experiments are often performed. The results of this

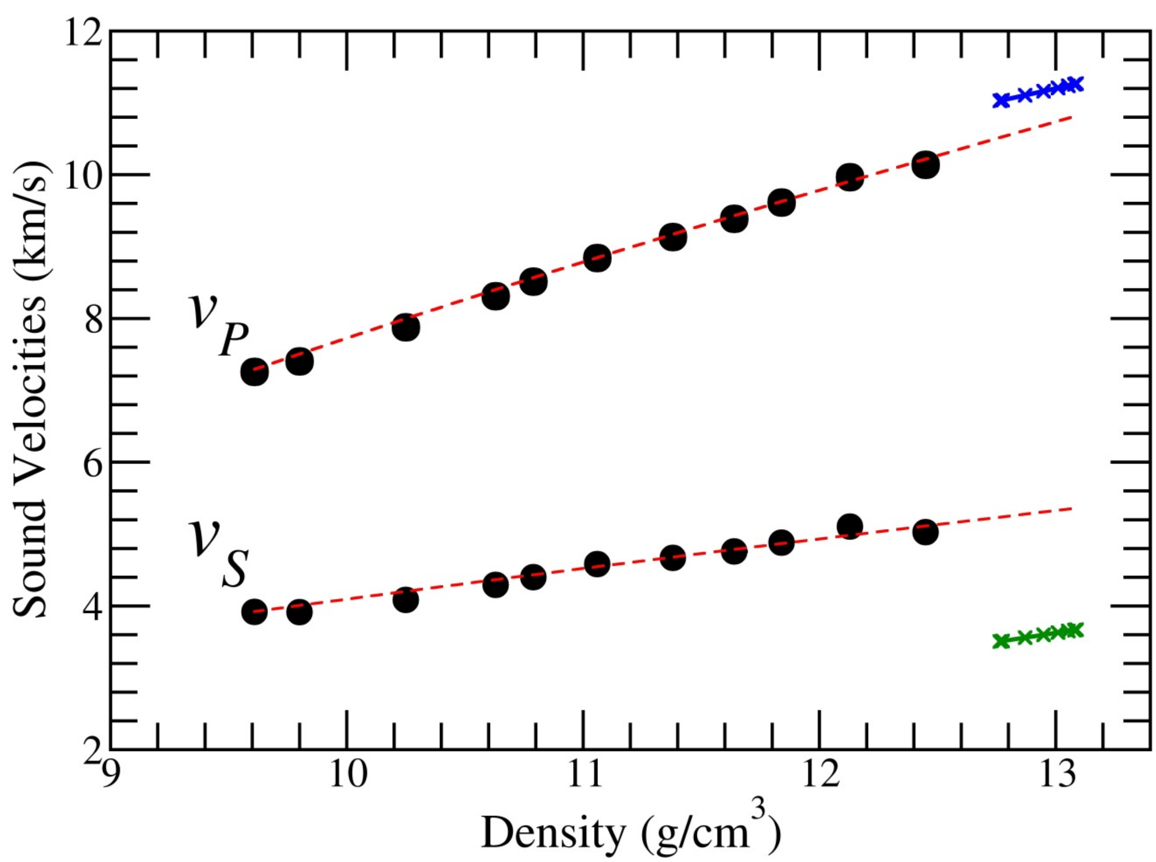

Figure 6.6. Density dependence of ε-Fe's sound velocities from our finite-strain model at 300 K, with PREM. Black circles give the density dependence of our measured compressional (v_p) and shear (v_s) sound velocities for ε-Fe. Red dashed lines give the result of our finite-strain model without temperature effects (T = 300 K; Section 6.3; Table 6.1), to confirm the appropriateness of the model. $v_p(\rho)$ and $v_s(\rho)$ from PREM are given by blue and green lines with x's, respectively (*Dziewonski and Anderson*, 1981).

simple finite-strain model are plotted as a function of density in Figure 6.6 as dashed red lines, where one can see that they agree well with our measured $v_p(\rho)$ and $v_s(\rho)$ at each compression point (filled circles). For comparison, we also include values for $v_p(\rho)$ and $v_s(\rho)$ from PREM as blue and green lines with X's, respectively.

Given the good agreement in Figure 6.6, we can now explore temperature effects on ε-Fe's sound velocities via the same finite-strain model. We assign a new anchor point to coincide with our measurement at ρ = 11.84 ± 0.02 g/cm^3 (P = 133 ± 4 GPa), which is close to the pressure of the core–mantle boundary (CMB; 135 GPa). We assign values for the ambient-temperature elastic moduli (K_S, K_S', μ, μ') from a combination of our data and the Vinet EOS reported by *Dewaele et al.* (2006) as before (Table 6.1), and a temperature at the CMB of 4000 K, based on an inner–core boundary (ICB) temperature of 5800 K and an outer core adiabat with γ = 1.56 (*Jackson et al.*, 2012). In order to approximate the temperature-dependent input parameters for our finite-strain model, we turn to theoretical calculations of the high-temperature elastic properties of ε-Fe. We note that pressure and temperature effects on $\partial\mu/\partial T$ have only been addressed with theoretical calculations and are not well-known. We estimate the temperature derivative of the shear modulus at the conditions of our anchor point to be -0.045 GPa/K, based on an interpolation of values given for the elastic stiffness constants at select densities and temperatures in Table 1 of *Sha and Cohen* (2010b). We note that this value is fairly close to the experimental value determined by *Lin et al.* (2005) at a smaller density (10.25 g/cm^3) and lower temperature (T < 1700 K). Next, we approximate ε-Fe's thermal expansion coefficient (α) at 135 GPa and 4000 K to be $\sim 1.8\times10^{-5}$ K^{-1}, based on Figure 11 in *Alfè et al.* (2001). Finally, the temperature derivative of the bulk modulus is related to the Anderson-Grüneisen parameter

(δ_T) via

$$\delta_T = \left(\frac{\partial \ln \alpha}{\partial \ln V}\right) = -\frac{1}{\alpha K_T}\left(\frac{\partial K_T}{\partial T}\right)_P . \tag{6.1}$$

Using Equation (6.1) with $\alpha K_T \approx$ 12.5 MPa/K at 4000 K and ~135 GPa from Figure 12 in *Alfè et al.* (2001), and $\delta_T \approx$ 4.5 from Figure 7 in *Sha and Cohen* (2010a), we approximate $\left(\partial K_T/\partial T\right)_{135\ \mathrm{GPa}} \approx$ -0.056 GPa/K at 4000 K (Table 6.1).

The pressure dependence of the density and compressional and shear sound velocities produced from the finite-strain model based on an anchor point near the conditions of Earth's CMB and the aforementioned parameters are plotted in Figure 6.7 as dashed red lines. Gray dashed lines give the results of a similar model with the same values for the elastic moduli listed in the second column in Table 6.1, but with a lower CMB temperature of 3600 K and, in turn, an inner core temperature of 5400 K. This lower-bound temperature for the CMB is based on recent high-*PT* XRD experiments of an Fe-O-S alloy. Finally, $\rho(P)$, $v_p(P)$ and $v_s(P)$ from PREM are plotted as black, blue, and green lines with X's, respectively (*Dziewonski and Anderson*, 1981). We note that v_p and v_s from the finite-strain model are determined as a function of density; to plot all of the parameters versus pressure, we apply the relevant densities to the Vinet EOS reported by *Dewaele et al.* (2006) and correct for thermal pressure following the procedure described in Sections 3.3 and 3.5. We assume the inner core is isothermal (e.g., *Stixrude et al.*, 1997) with a temperature of 5800 K, which corresponds to the melting point of ε-Fe at the ICB determined by *Jackson et al.* (2012) using a combination of high-temperature synchrotron Mössbauer spectroscopy experiments and the melting curve shape and thermal pressure determined in Chapter 3.

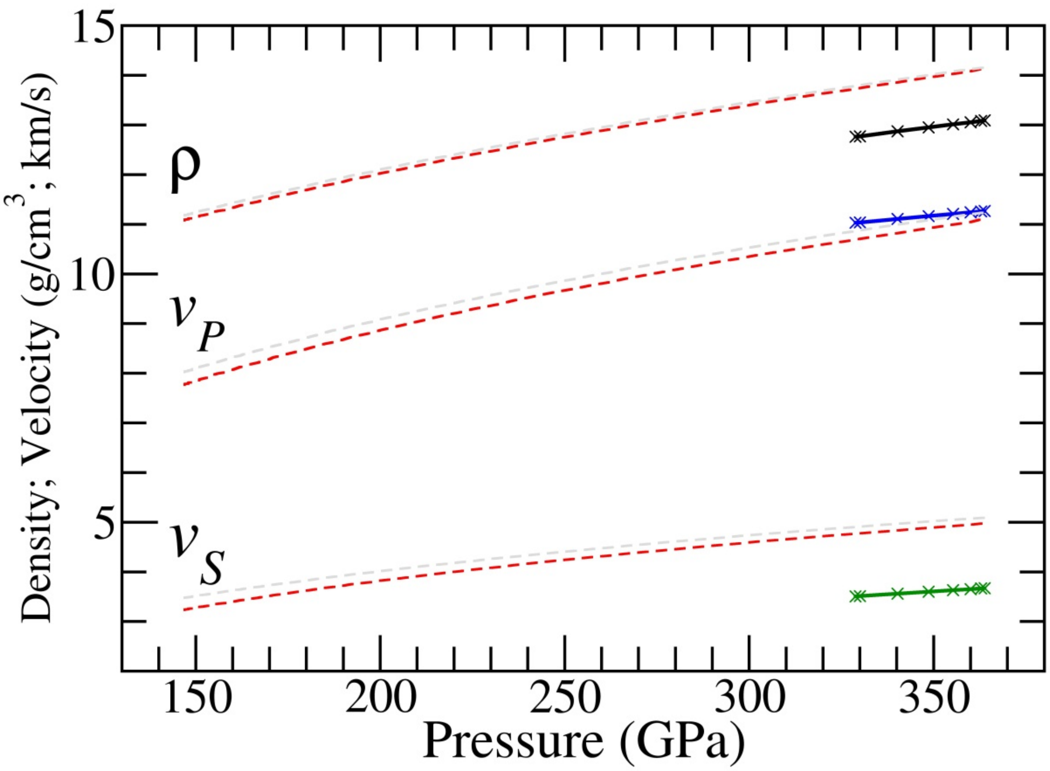

Figure 6.7. Modeled pressure dependence of ε-Fe's density and sound velocities from our finite strain model, with PREM. Red dashed lines give results for the density (ρ) and compressional (v_p) and shear (v_p) sound velocities of ε-Fe from our finite-strain model with an anchor point near the conditions expected for Earth's core–mantle boundary (133 GPa and 4000 K; Section 6.3; Table 6.1). Grey dashed lines correspond to a lower bound CMB temperature of 3600 K, based on the results of *Terasaki et al.* (2011). Densities from the model are converted to pressure using the Vinet EOS reported by *Dewaele et al.* (2006) and our thermal pressure correction described in Chapter 3, assuming an inner core temperature of 5600 K. $\rho(P)$, $v_p(P)$, and $v_s(P)$ from PREM are given by black, blue, and green lines with x's, respectively (*Dziewonski and Anderson*, 1981).

Figure 6.7 reveals fairly good agreement between the modeled high-*PT* compressional sound velocities of ε-Fe and those of the inner core, but noticeably different slopes for $v_p(P)$. By contrast, the predicted densities and shear sound velocities from the finite-strain model have very similar slopes as those from PREM, but the modeled values are significantly larger: ~8% and ~4.5%, respectively, throughout the inner core. We note that our reported density contrast (i.e., the core density deficit, or CDD) is from the mass of our 95% isotopically enriched samples (m = 56.95 g/mol), which was the mass (density) used to determine our sound velocities for ε-Fe and all of the input parameters for the finite-strain model that were based on our data. Scaling the densities in the finite-strain model by the ratio of the mass for the natural isotopic distribution of iron (55.845 g/mol) to that of our ^{57}Fe samples and recalculating the CDD, one obtains a constant value of ~5.8%, which agrees well with our previously determined value of 5.5 ± 0.2 in Section 3.5. Finally, we note that the nearly constant value of the CDD throughout the inner core—assuming a constant temperature in the layer—is consistent with a chemically homogeneous inner core.

\

Table 6.1. Input parameters for our finite-strain model.

	Figure 6.6	**Figure 6.7**
Anchor Point Values[a]		
T (K)	300	4000
P (GPa)	31(2)	133(4)
ρ (g/cm^3)	9.61(3)	11.84(2)
K (GPa)	309	718
K'	4.47	3.87
μ (GPa)	147.7(1.3)	282.3(6.2)
μ'	1.5	1.16
Thermal Properties[b]		
α (10^{-5} K^{-1})	--	1.8
$\partial K/\partial T$ (GPa/K)	--	-0.056
$\partial \mu/\partial T$ (GPa/K)	--	-0.045

[a]Parameters that define the anchor points for our finite-strain models. Temperatures (T) are assigned to 300 K (Figure 6.6) to confirm that the finite strain model matches our data well; and to an approximate temperature on the core side of the CMB (Figure 6.7) to investigate temperature effects on our measured sound velocities. Pressures (P) and densities (ρ) correspond to two of our measured compression points (Tables 2.1 and 2.2). The adiabatic bulk modulus (K) and its pressure derivative (K') are determined from the Vinet EOS reported by *Dewaele et al.* (2006) and our measured thermodynamic properties (Section 5.5); the shear modulus (μ) and its pressure derivative (μ') are determined from our measured densities and shear sound velocities following $v_s^2 = \mu/\rho$.
[b]The thermal expansion coefficient (α) and temperature derivatives of the bulk modulus $(\partial K/\partial T)$ and shear modulus $(\partial \mu/\partial T)$ are only relevant for T > 300 K, and are approximated as described in the text (Section 6.3).

Therefore, our finite-strain models gives no indication that a chemical gradient exists in the inner core, as might be expected if the light elements in the core preferentially enter the liquid phase, resulting in an outer core that becomes increasingly enriched in light elements with time and, in turn, an inner core that hosts more light elements with increasing radius.

Putting this all together, our approximate finite-strain model for the high-*PT* elastic properties of ε-Fe suggests that its compressional sound velocities match those inferred for Earth's solid inner core fairly well, while its density and shear sound velocities are larger than those of the core. Based on our discussion in Section 6.2, one possible mechanism for resolving this discrepancy is via the addition of light elements, which tend to have only minor effects on the compressional sound velocity of pure iron, but can significantly lower both its density and shear sound velocities. Another possible mechanism would be a higher temperature in the inner core, but we note that temperature is also expected to affect compressional sound velocities (e.g., *Lin et al.*, 2005). Therefore, temperature alone cannot explain our estimates for the shear sound velocity and density contrasts, suggesting that light elements must be present in Earth's inner core to match seismic observations.

Finally, while our finite strain model provides a good qualitative investigation of temperature effects on the sound velocities of ε-Fe, we note that it is highly sensitive to the temperature derivatives of the high-pressure elastic moduli, which are not well-known. As previously discussed, we rely on theoretical calculations for these values because they are extremely difficult to access experimentally at the conditions of Earth's core. Results from a variety of first-principles calculations seem to agree that the shear modulus decreases with increasing temperature $\left(\partial\mu/\partial T < 0\right)$ at core pressures, although the magnitude of this derivative varies from study to study (*Steinle-Neumann et al.*, 2001; *Vočadlo et al.*, 2009;

Sha and Cohen, 2010b). The same studies also produce very discrepant values for the temperature derivative of the bulk modulus: *Vocadlo et al.* (2009) predict $\partial K/\partial T < 0$—which is consistent with the value used in our finite strain model (Table 6.1)—but both *Steinle-Neumann et al.* (2001) and *Sha and Cohen* (2010b) find $\partial K/\partial T > 0$ as a result of the fact that *c* / *a* increases rapidly at high temperatures. Therefore, additional work is needed to better understand the behavior of the elastic constants of ε-Fe at high-*PT* conditions before more quantitative conclusions can be made about the effects of temperature on the sound velocities of ε-Fe.

6.4 Concluding Remarks

In this thesis, we have investigated the thermoelastic and vibrational thermodynamic properties of the high-pressure hexagonal close-packed phase of iron (ε-Fe) up to an outer core pressure of 171 GPa, for the purpose of improving our understanding of Earth's iron-rich core. In particular, we used nuclear resonant inelastic x-ray scattering and *in situ* x-ray diffraction experiments in a diamond-anvil cell to directly probe the volume dependence of the total phonon density of states (DOS) of ε-Fe. In turn, we determined a variety of vibrational thermodynamic parameters, whose volume dependences are intimately related to many important properties of Earth's core. The major conclusions of this thesis include

- The volumetric derivative of ε-Fe's vibrational free energy is directly related to its vibrational thermal pressure, which we use to determine the total thermal pressure by accounting for temperature and electronic effects. Assuming an inner–core boundary (ICB) temperature of 5600 K, we determine a total thermal pressure of

56 GPa at this boundary and a corresponding core-density deficit of 5.5 ± 0.2%. We note that this new tight constraint on the amount of light elements present in Earth's solid inner core has important implications for the relative importance of chemical versus thermal buoyancy in generating the geodynamo, and in estimates of the melting (freezing) point depression at the inner–core boundary (Chapter 3).

- The volume dependence of ε-Fe's Lamb-Mössbauer factor is related to the mean-square atomic displacement and, in turn, the melting curve shape via Gilvarry's reformulation of Lindemann's melting criterion. By anchoring our determined melting curve shape with established melting points for ε-Fe and accounting for both temperature effects and the previously mentioned thermal pressure, we determine a melting temperature of ε-Fe at 330 GPa of 5600 ± 200 K. This serves as an estimate for the temperature at the ICB, where Earth's iron-rich solid inner core and liquid outer core are in contact (Chapter 3).
- The volume dependence of the phonon DOS is directly related to the definition of the vibrational Grüneisen parameter (γ_{vib}), which we determine using a generalized-scaling analysis of the phonon DOS and the common parameterization, $\gamma_{vib}(V) = \gamma_{vib,0}(V/V_0)^q$. We find an ambient pressure $\gamma_{vib,0} = 2.0 \pm 0.1$ for a range of $q = 0.8$ to 1.2 at 300 K, which provides a self-consistent check on the vibrational thermal pressure and melting curve shape previously described (Chapter 4).
- The reduced isotopic partition function ratios (β-factors) of ε-Fe are directly related to its vibrational kinetic energy. We investigated ε-Fe's β-factors as a function of pressure and temperature, and found that the available resolution does not permit determination of isotopic shifts at the temperatures expected for Earth's mantle. In

addition, we emphasize that the β-factors reported here are for solid iron and are expected to differ significantly from the corresponding values for liquid iron, where the latter are more closely related to discussions of core formation (Chapter 5).

- The volumetric derivative of the vibrational entropy is directly related to the product of the vibrational thermal expansion coefficient (α_{vib}) and the isothermal bulk modulus. Using existing equation of state parameters, we determine α_{vib}(300 K) ranges from 1.84 ± 0.01 10^{-5} K^{-1} to 0.67 10^{-5} K^{-1} over our experimental compression range. Together with our γ_{vib}, this result provides the means for converting between isothermal and adiabatic bulk moduli, which is necessary for determining accurate sound velocities for ε-Fe (Chapter 5).
- A parabolic fit of the low-energy region of the phonon DOS provides ε-Fe's Debye sound velocity via our measured sound velocities. In turn, the combination of our Debye sound velocities with our measured density, γ_{vib}, and α_{vib}, and established isothermal bulk moduli gives ε-Fe's compressional and shear sound velocities at 300 K. Comparing our measured sound velocities with those reported for iron alloys, we find that an important next step is to extend the compression range and improve the statistical quality of sound velocity data for iron alloys, in order to allow for more quantitative conclusions about the effects of alloying on the sound velocities of ε-Fe. Finally, we compare our measured sound velocities with seismic observations via third-order finite-strain analysis and estimates for the thermal properties of ε-Fe. From the modeled high-temperature behavior of our sound velocities, we find fairly good agreement between ε-Fe's compressional sound velocities and those inferred for the inner core from the Preliminary Reference

Earth Model; however, ε-Fe's density and shear sound velocities are ~6% and 4.5% larger than those of the core, respectively, further suggesting the presence of light elements in the solid inner core. We note that a better understanding of the high-pressure and temperature behavior of ε-Fe's elastic moduli is necessary in order to make more quantitative conclusions about the effects of temperature on the sound velocities of ε-Fe.